Mechanics of Materials 143 (2020) 103320

Contents lists available at ScienceDirect

Mechanics of Materials

journal homepage: www.elsevier.com/locate/mechmat

Research paper

Poroelastic effects on steady state crack growth in polymer gels under plane stress

Yalin Yu, Chad M. Landis, Rui Huang*

Department of Aerospace Engineering and Engineering Mechanics, University of Texas, Austin, TX 78712

ARTICLE INFO

Keywords:
Gels
Fracture
Poroelasticity
Cohesive zone model

ABSTRACT

Fracture experiments on polymer gels are often conducted with thin specimens, which are close to plane stress in two-dimensional models. However, many of the previous theoretical and numerical studies on fracture of polymer gels have assumed plane strain conditions. The subtle differences between the plane stress and plane strain conditions are elucidated in this paper based on a linear poroelastic formulation for polymer gels, including the asymptotic crack-tip fields and finite element simulations of steady-state crack growth in long strip specimens. Moreover, a poroelastic cohesive zone model is adopted to study the rate-dependent fracture process of polymer gels. It is found that, without the cohesive zone model, the normalized crack-tip energy release rate at the fast crack limit is greater than the slow crack limit, suggesting reduced poroelastic toughening for fast crack growth under plane stress conditions, while the two limits are identical under plane strain conditions. With a solvent-permeable cohesive zone for the case of immersed specimens, solvent diffusion within the cohesive zone enhances the poroelastic toughening significantly as the crack speed increases, leading to a rate-dependent traction-separation relation. On the other hand, with no solvent diffusion in the cohesive zone for the not-immersed case, the poroelastic toughening effect diminishes as the crack speed increases. Based on the present study, the intrinsic steady-state fracture toughness of a poroelastic gel can be determined using long-strip pure-shear specimens, which in general is smaller than the applied energy release rate.

1. Introduction

Consisting of cross-linked polymer chains and a large content of solvent molecules (e.g., water), polymer gels are often brittle with a fracture toughness on the order of 10 J/m^2 (Long and Hui, 2016). To enhance the fracture toughness of polymer gels for engineering applications such as sensing and actuating components in soft machines and soft robotics, many types of tough gels have been developed over the last decade, with the reported fracture toughness up to 10^4 J/m^2 (Gong et al., 2003; Sun et al., 2012; Zhao, 2014; Creton, 2017). These material developments have motivated a series of theoretical and computational studies on the fracture mechanics of polymer gels (Wang and Hong, 2012; Hui et al., 2013; Bouklas et al., 2015; Noselli et al., 2016; Long et al., 2016; Mao and Anand, 2018; Guo et al., 2018; Yang and Lin, 2018; Yu et al., 2018a, 2018b; Liu et al., 2019).

Many gels exhibit rate-dependent fracture behaviors (Baumberger et al., 2006; Seitz et al., 2009; Lefranc and Bouchaud, 2014; Forte et al., 2015; Long and Hui, 2016). In particular, Baumberger et al. (2006) found that the measured energy release rate increased with increasing crack speed for steady-state crack growth in gelatin gels by pure-shear experiments (so-called "velocity toughening"). Similar results were reported for other gels (Seitz et al., 2009; Lefranc and Bouchaud, 2014). The underlying mechanisms for the rate dependent fracture of polymer gels may be multifaceted with three primary suspects: rate-dependent fracture processes at the crack tip, viscoelastic effects, and poroelastic effects. The present study focuses on the poroelastic effects on steady-state crack growth, including solvent diffusion in the bulk of the gel and potentially in a cohesive zone ahead of the crack tip. Previously, Noselli et al. (2016) presented a theoretical and numerical study on steady-state crack growth in polymer gels, based on linear poroelasticity. They predicted a poroelastic toughening effect and proposed a linear poroelastic cohesive zone model. In our previous study (Yu et al., 2018b), we presented an asymptotic analysis of the crack-tip fields for steady-state crack growth in polymer gels and numerical results for a semi-infinite crack in a long strip specimen. The results are consistent with Noselli et al. (2016) at the limit of "fast" crack growth when the characteristic diffusion length scale is much smaller than the specimen size (small-scale diffusion). Both of these studies assumed plane strain conditions. However, in experiments (e.g., Baumberger et al., 2006; Lefranc and Bouchaud, 2014), thin specimens

* Corresponding author.
E-mail address: ruihuang@mail.utexas.edu (R. Huang).

https://doi.org/10.1016/j.mechmat.2020.103320
Received 28 May 2019; Received in revised form 9 January 2020; Accepted 10 January 2020
Available online 17 January 2020
0167-6636/

are commonly used, which can be modelled more accurately with plane stress conditions instead of plane strain. To elucidate the subtle differences between the plane stress and plane strain conditions, we present in this paper asymptotic crack-tip fields and finite element simulations of steady-state crack growth in polymer gels under plane stress conditions. Moreover, a nonlinear poroelastic cohesive zone model is proposed to study the rate-dependent fracture process of polymer gels.

The remainder of this paper is organized as follows. Section 2 summarizes the governing equations of linear poroelasticity under plane stress conditions. A long strip model of steady state crack growth is presented in Section 3, followed by the asymptotic plane-stress crack-tip fields in Section 4. In Section 5, we develop a nonlinear poroelastic cohesive zone model. Similar to the previous work (Yu et al., 2018b), a stabilized finite element method was implemented (Appendix A), and numerical results are presented and discussed in Section 6. Section 7 concludes the present study with a brief summary.

2. Linear poroelasticity under plane stress

The linear poroelastic formulation can be derived from the generally nonlinear theory for polymer gels (Bouklas and Huang, 2012), which has allowed asymptotic analyses of the crack-tip fields under plane strain conditions in the previous studies (Yu et al., 2018a, 2018b). Here, we briefly summarize the formulation of linear poroelasticity for gels and note the differences between plane-stress and plane-strain conditions.

Let the gel be stress free and isotropically swollen in the initial state, where the solvent in the gel has a chemical potential, $\mu = \mu_0$, in equilibrium with an external solution. Correspondingly, the initial solvent concentration in the gel (number of solvent molecules per unit volume) is: $c_0 = (1 - \lambda_0^{-3})/\Omega$, where Ω is the volume of each solvent molecule and λ_0 is the linear swelling ratio of the gel relative to dry state of the polymer network. The relationship between the swelling ratio (λ_0) and the chemical potential (μ_0) can be obtained from the nonlinear theory (Hong et al., 2008; Kang and Huang, 2010). Considering small deformation from the initial state with a displacement field u_i, the linear strain field is

$$\varepsilon_{ij} = \frac{1}{2}\left(\frac{\partial u_i}{\partial x_j} + \frac{\partial u_j}{\partial x_i}\right). \tag{2.1}$$

The volumetric part of the strain is related to the change of solvent concentration, i.e.,

$$\varepsilon_{kk} = \Omega(c - c_0), \tag{2.2}$$

where c is the solvent concentration in the deformed state.

The Cauchy stress in the gel is related to the strain and chemical potential as:

$$\sigma_{ij} = 2G\left(\varepsilon_{ij} + \frac{\nu}{1-2\nu}\varepsilon_{kk}\delta_{ij}\right) - \frac{\mu - \mu_0}{\Omega}\delta_{ij}, \tag{2.3}$$

where G is shear modulus and ν is Poisson's ratio.[1]

For quasi-static problems, the linearized mechanical equilibrium equation (assuming no body force) is:

$$\frac{\partial \sigma_{ij}}{\partial x_j} = 0, \tag{2.4}$$

and the linearized equation for solvent diffusion is:

$$\frac{\partial c}{\partial t} + \frac{\partial j_k}{\partial x_k} = 0, \tag{2.5}$$

where the diffusion flux is proportional to the gradient of chemical potential as:

$$j_k = -M_0\frac{\partial \mu}{\partial x_k}, \tag{2.6}$$

with a constant mobility M_0.

Correspondingly, the linearized boundary conditions are:

$$\sigma_{ik}n_k = \tau_i \text{ and } j_k n_k = -\omega, \tag{2.7}$$

where n_k is the outward unit normal vector on the boundary, τ_i is the traction, and ω is the in-flux of the solvent across the boundary.

Under plane stress conditions, $\sigma_{33} = 0$ and by Eq. (2.3) we obtain

$$\varepsilon_{33} = -\frac{\nu}{1-\nu}(\varepsilon_{11} + \varepsilon_{22}) + \frac{1-2\nu}{1-\nu}\frac{(\mu - \mu_0)}{2G\Omega}. \tag{2.8}$$

Then, Eq. (2.2) becomes

$$\Omega(c - c_0) = \frac{1-2\nu}{1-\nu}(\varepsilon_{11} + \varepsilon_{22}) + \frac{1-2\nu}{1-\nu}\frac{(\mu - \mu_0)}{2G\Omega}. \tag{2.9}$$

Therefore, the solvent concentration c not only depends on the in-plane normal strains but also depends on the chemical potential under plane stress conditions. In contrast, the solvent concentration depends on the in-plane normal strains only under plane strain conditions ($\varepsilon_{33} = 0$). This subtle difference turns out to be consequential in the subsequent analysis of the poroelastic crack-tip fields. It should be noted that, under plane stress conditions, both the solvent concentration and chemical potential are assumed to be two-dimensional (2D) fields, with no solvent diffusion in the out-of-plane direction. This implies that the surfaces of the thin specimen are impermeable to solvent diffusion. On the other hand, if the surfaces are permeable and in contact with an environment of a constant chemical potential, solvent diffusion in the out-of-plane direction would take very little time to maintain the chemical equilibrium so that the chemical potential of solvent would remain constant everywhere in the gel. In this case, the gel behaves like an elastic material, and the 2D plane-stress elasticity solution (with drained Poisson's ratio) would be applicable. Since the solution for plane-stress elasticity is well known, here we present a solution for plane-stress poroelasticity with 2D in-plane diffusion. The real specimens (with finite thickness) could be more complicated, and a full 3D analysis would be needed to determine the validity of the 2D approximations, which however is beyond the scope of the present study.

With Eq. (2.9), Eq. (2.3) can be rewritten for the in-plane stress components in terms of the in-plane strain and chemical potential as

$$\sigma_{\alpha\beta} = 2G\left[\varepsilon_{\alpha\beta} + \frac{\nu}{1-\nu}(\varepsilon_{11} + \varepsilon_{22})\delta_{\alpha\beta}\right] - \frac{1-2\nu}{1-\nu}\frac{\mu - \mu_0}{\Omega}\delta_{\alpha\beta}, \tag{2.10}$$

where $\alpha, \beta = 1, 2$ are the indices for the 2D in-plane components.

By inserting Eq. (2.10) into (2.4), we obtain

$$\frac{\partial^2 u_\alpha}{\partial x_\beta \partial x_\beta} + \frac{1+\nu}{1-\nu}\frac{\partial^2 u_\beta}{\partial x_\beta \partial x_\alpha} = \frac{1-2\nu}{1-\nu}\frac{1}{G\Omega}\frac{\partial \mu}{\partial x_\alpha}, \tag{2.11}$$

which leads to

$$\nabla^2 \varepsilon_{\alpha\alpha} = \frac{1-2\nu}{2G\Omega}\nabla^2 \mu, \tag{2.12}$$

with $\nabla^2 = \frac{\partial^2}{\partial x_1^2} + \frac{\partial^2}{\partial x_2^2}$ for 2D analyses.

Combining Eqs. (2.9) and (2.12), we obtain

$$\nabla^2 \mu = \frac{\Omega^2 G}{1-2\nu}\nabla^2 c. \tag{2.13}$$

With Eqs. (2.6) and (2.13), Eq. (2.5) becomes

$$\frac{\partial c}{\partial t} = D_s^* \nabla^2 c, \tag{2.14}$$

where $D_s^* = \frac{\Omega^2 G M_0}{1-2\nu}$ is the effective diffusivity under plane stress conditions. Note that, under plane strain conditions, the effective diffusivity

[1] The Poisson's ratio here is often called *drained* Poisson's ratio in linear poroelasticity (Biot, 1941; Atkinson and Craster, 1991). The *undrained* Poisson's ratio is 0.5 in the present formulation as a result of Eq. (2.2).

is: $D^* = \frac{2(1-\nu)}{1-2\nu}\Omega^2 G M_0$, which is the same for 3D problems (Hui et al., 2006; Hu et al., 2011). Thus, the effective diffusivity is reduced under plane stress conditions, i.e., $D_s^* = \frac{D^*}{2(1-\nu)} < D^*$ (for $\nu < 0.5$).

As in linear elasticity, the equilibrium Eq. (2.4) may be solved by using the Airy's stress function ψ under plane strain or plane stress conditions, with $\sigma_\theta = \frac{\partial^2\psi}{\partial r^2}$, $\sigma_r = \frac{1}{r^2}\frac{\partial^2\psi}{\partial\theta^2} + \frac{1}{r}\frac{\partial\psi}{\partial r}$, and $\sigma_{r\theta} = -\frac{\partial}{\partial r}(\frac{1}{r}\frac{\partial\psi}{\partial\theta})$ as usual. Then, with the poroelastic stress-strain relation in Eq. (2.3), the strain compatibility condition requires that

$$\nabla^2\nabla^2\psi = -\beta\Omega G\nabla^2 c, \tag{2.15}$$

where $\beta = 1$ for plane stress and $\beta = 2$ for plane strain.

Therefore, under plane stress conditions, we may solve Eq. (2.14) for the solvent concentration and then solve Eq. (2.15) for the stress function. The chemical potential can then be obtained from Eq. (2.3) as:

$$\mu - \mu_0 = \frac{2(1+\nu)G\Omega^2}{3(1-2\nu)}(c - c_0) - \frac{\Omega}{3}\nabla^2\psi \tag{2.16}$$

for plane stress ($\sigma_{kk} = \sigma_r + \sigma_\theta = \nabla^2\psi$), while for plane strain we have (Yu et al., 2018a, 2018b):

$$\mu - \mu_0 = \frac{G\Omega^2}{1-2\nu}(c - c_0) - \frac{\Omega}{2}\nabla^2\psi \tag{2.17}$$

We note the differences between plane stress and plane strain for linear poroelasticity in Eqs. (2.9), (2.10), (2.14), (2.15), and (2.16).

3. A plane-stress steady-state crack growth model

In the present study, we consider steady-state crack growth in a long strip specimen of a polymer gel under plane stress conditions, as opposed to plane strain conditions in a previous work (Yu et al., 2018b). As shown in Fig. 1, the strip width is $2h$, with a semi-infinite crack lying in the mid-plane. Subjected to an opening displacement $\pm\Delta$ applied to the upper and lower surfaces of the strip, the crack grows and reaches a steady state with a constant crack speed $\dot{a}$. Similar specimens have been used in experiments for various materials including gels (Rivlin and Thomas, 1953; Long and Hui, 2016). In most cases, the specimen is a thin sheet with a small thickness in comparison to the width, commonly known as the pure shear test, which is close to the plane stress conditions assumed in this study.

Adopt a moving coordinate system with the origin at the crack tip (Fig. 1). With respect to the moving coordinate (for an observer traveling with the crack tip), the mechanical equilibrium equation remains the same as in Eq. (2.4), but the equation for solvent concentration is time-independent as $\frac{\partial}{\partial t} = -\dot{a}\frac{\partial}{\partial x_1}$ with a constant steady-state crack speed. Thus, Eq. (2.14) becomes

$$-\dot{a}\frac{\partial c}{\partial x_1} = D_s^*\nabla^2 c. \tag{3.1}$$

A steady-state diffusion length scale emerges from Eq. (3.1), namely

$$l_{SS} = \frac{D_s^*}{\dot{a}}, \tag{3.2}$$

which is inversely proportional to the crack speed.

The steady state crack model (Fig. 1) has two relevant length scales: the specimen half-width h and the steady-state diffusion length l_{SS}. The ratio between the two length scales defines a dimensionless number

$$\mathrm{Pe} = \frac{h}{l_{SS}} = \frac{\dot{a}h}{D_s^*}, \tag{3.3}$$

which is called the Péclet number for advection-diffusion problems (Franca et al., 1992). Note that the Péclet number is slightly different under plane strain conditions due to the difference in the effective diffusivity (Yu et al., 2018b).

If the specimen is made of a material that is linearly elastic and incompressible, the energy release rate for steady state crack growth in the pure shear test is simply:

$$J_e = 4G\varepsilon_\infty^2 h. \tag{3.4}$$

where $\varepsilon_\infty = \Delta/h$. Correspondingly, the stress intensity factor at the crack tip under plane stress conditions is:

$$K_e = 2G\varepsilon_\infty\sqrt{3h}. \tag{3.5}$$

Note that, while the steady-state energy release rate is the same for plane stress and plane strain (Yu et al., 2018a), the stress intensity factors are slightly different.

For a poroelastic gel specimen, part of the energy supplied by the remote loading is dissipated due to solvent diffusion around the crack tip. Consequently, the crack-tip energy release rate is generally lower than that in Eq. (3.4) and may depend on the crack speed. Similarly, the stress intensity factor in a linearly poroelastic specimen is generally lower than Eq. (3.5), an effect known as poroelastic shielding (Atkinson and Craster, 1991; Hui et al., 2013). To calculate the crack-tip energy release rate in poroelastic gels, a modified J-integral was derived by Bouklas et al. (2015) in a nonlinear setting, and for linear poroelasticity it reduces to:

$$J^* = \int_C \left(\hat{\phi}n_1 - \sigma_{\alpha\beta}n_\beta\frac{\partial u_\alpha}{\partial x_1}\right)d\Gamma + \int_A (c - c_0)\frac{\partial\mu}{\partial x_1}dA, \tag{3.6}$$

where A is the area enclosed by the contour C around the crack tip and $\hat{\phi}$ is the free energy density function for linear poroelasticity:

$$\hat{\phi} = G\left[\varepsilon_{ij}\varepsilon_{ij} + \frac{\nu}{1-2\nu}(\varepsilon_{kk})^2\right] - (\mu - \mu_0)(c - c_0). \tag{3.7}$$

Note that $\varepsilon_{ij}\varepsilon_{ij} = \varepsilon_{\alpha\beta}\varepsilon_{\alpha\beta} + \varepsilon_{33}^2$ under plane stress conditions, where ε_{33} is related to the in-plane strain components and the chemical potential by Eq. (2.8).

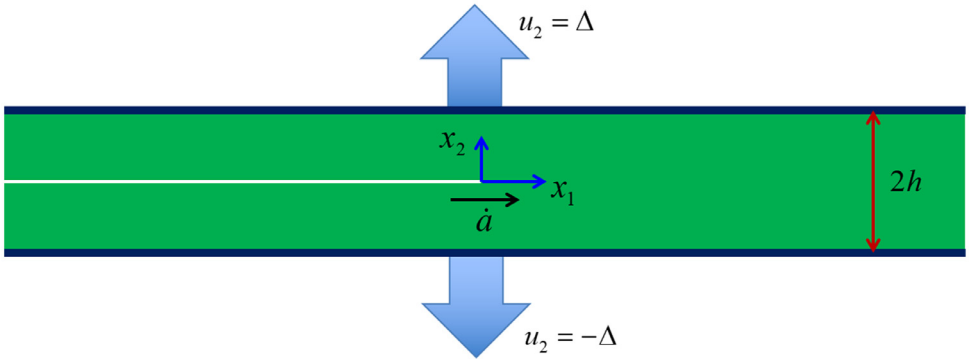

Fig. 1. Schematic of a long strip specimen with steady-state crack growth in the x_1 direction.

4. Asymptotic crack-tip fields under plane stress

Under plane stress conditions, we solve Eqs. (3.1) and (2.15) to obtain an asymptotic solution for the steady-state crack-tip fields in a linearly poroelastic material. The solution procedure is the same as in the previous study for plane strain conditions (Yu et al., 2018b), aside from a few different parameters such as the effective diffusivity (D_s^* versus D^*). Here, we present the asymptotic solution without repeating the lengthy derivation and emphasize the differences between plane stress and plane strain conditions.

For both plane strain and plane stress, the leading terms of the crack-tip stress field (mode I only) are given by

$$\sigma_{ij} = \frac{K_I}{\sqrt{2\pi r}} f_{ij}(\theta) + T\delta_{1i}\delta_{1j} + o\left(\sqrt{\frac{r}{l_{SS}}}\right), \tag{4.1}$$

where as in linear elastic fracture mechanics (LEFM), K_I is the stress intensity factor, T is the T-stress, and

$$f_{11} = \cos\left(\frac{\theta}{2}\right)\left[1 - \sin\left(\frac{\theta}{2}\right)\sin\left(\frac{3\theta}{2}\right)\right], \tag{4.2}$$

$$f_{22} = \cos\left(\frac{\theta}{2}\right)\left[1 + \sin\left(\frac{\theta}{2}\right)\sin\left(\frac{3\theta}{2}\right)\right], \tag{4.3}$$

$$f_{12} = \cos\left(\frac{\theta}{2}\right)\sin\left(\frac{\theta}{2}\right)\cos\left(\frac{3\theta}{2}\right). \tag{4.4}$$

Correspondingly, the singular part of the crack-tip strain field and the leading term of the displacement field are identical to those in the linear elastic solution. In particular, the crack opening displacement is given by:

$$u_2(r, \theta = \pm\pi) = \pm\frac{4K_I}{\tilde{E}}\sqrt{\frac{r}{2\pi}} + o\left(\frac{r}{l_{SS}}\right), \tag{4.5}$$

where $\tilde{E} = 2G/(1-\nu)$ for plane strain and $\tilde{E} = 2G(1+\nu)$ for plane stress.

The asymptotic crack-tip field of the solvent concentration is given by

$$(c - c_0)\Omega = h_1(\nu)\frac{K_I}{G\sqrt{2\pi r}}\cos\left(\frac{\theta}{2}\right) + c_1\Omega + o\left(\sqrt{\frac{r}{l_{SS}}}\right), \tag{4.6}$$

where $h_1(\nu) = 1 - 2\nu$ for plane strain and $h_1(\nu) = (1-2\nu)/(1+\nu)$ for plane stress.

The asymptotic field of the chemical potential is:

$$\mu = \mu_{tip} - h_2(\nu)\frac{\Omega K_I}{\sqrt{2\pi l_{SS}}}\left[\cos\left(\frac{3\theta}{2}\right) + \kappa\cos\left(\frac{\theta}{2}\right)\right]\left(\frac{r}{l_{SS}}\right)^{1/2} + o\left(\frac{r}{l_{SS}}\right), \tag{4.7}$$

where $h_2(\nu) = (1-\nu)/2$ for plane strain and $h_2(\nu) = 1/(4(1+\nu))$ for plane stress.

Two types of chemical boundary conditions are considered for the crack faces. If the crack faces are in equilibrium with an external solution (e.g., water), the chemical potential must be zero on the crack faces ($\theta = \pm\pi$) and at the crack tip, i.e., $\mu_{tip} = 0$; such a crack is called immersed. Alternatively, if the crack faces are impermeable to solvent diffusion so that the flux across the crack faces is zero, $\kappa = 3$ is required in Eq. (4.7) for the not-immersed case.

The constant term in solvent concentration is related to the T-stress and the crack-tip chemical potential as:

$$\Omega c_1 = \begin{cases} \frac{1-2\nu}{2G}\left(\frac{3\mu_{tip}}{\Omega} + T\right), & \text{plane stress} \\ \frac{1-2\nu}{2G(1+\nu)}\left(\frac{2\mu_{tip}}{\Omega} + T\right), & \text{plane strain} \end{cases} \tag{4.8}$$

Thus, for either the immersed or not-immersed cases, there are three independent parameters for the poroelastic crack-tip fields: K_I, T, and κ (immersed) or μ_{tip} (not-immersed).

With the asymptotic crack-tip fields, it can be shown that the relationship between the modified J-integral in Eq. (3.6) and the stress intensity factor is identical to that in LEFM (Yu et al., 2018b), namely

$$J^* = \frac{K_I^2}{\tilde{E}}. \tag{4.9}$$

We note that the plane-stress crack-tip solution should be limited to the region with r greater than the specimen thickness. In the present study, with the steady-state diffusion length scale l_{SS}, the plane-stress solution is limited to the cases where the specimen thickness is small compared to the diffusion length, so that the effect of triaxiality is confined within a small region near the crack tip.

5. A poroelastic cohesive zone model

To describe the micromechanics of fracture in gels, Noselli et al. (2016) proposed a linear poroelastic cohesive zone model considering both deformation and solvent diffusion in the cohesive zone. Here, we present a slightly different cohesive zone model for gels based on a free energy density function and a nonlinear diffusion equation within the cohesive zone. Cohesive zone models have been commonly adopted in nonlinear fracture mechanics to describe the fracture processes at the crack tip, typically with nonlinear traction-separation relations (Hutchinson and Evans, 2000). Interestingly, it is found that solvent diffusion within the cohesive zone leads to rate-dependent traction-separation relations, with significantly enhanced poroelastic toughening as the crack speed increases.

Consider the immersed case first, where the cohesive zone is permeable to solvent diffusion (Fig. 2). Similar to the free energy density function of polymer gels in the bulk, we assume a free energy density function (per unit area) for the solvent-permeable cohesive zone as:

$$\phi_c(\delta, \mu) = \frac{1}{2}k\delta^2 - \frac{\mu}{\Omega}\delta, \tag{5.1}$$

where δ is the opening displacement, μ is the chemical potential of the solvent in the cohesive zone, and k is the stiffness of the cohesive zone (assumed to be a constant in the present study). The opening stress and the solvent concentration in the cohesive zone can then be obtained as:

$$\sigma_{22} = \frac{\partial\phi_c}{\partial\delta} = k\delta - \frac{\mu}{\Omega}, \tag{5.2}$$

$$\zeta = -\frac{\partial\phi_c}{\partial\mu} = \frac{\delta}{\Omega}, \tag{5.3}$$

where ζ is the number of solvent molecules per unit area. Note that Eqs. (5.2) and (5.3) are essentially the same as those in Noselli et al. (2016).

Solvent transport in the permeable cohesive zone must satisfy mass

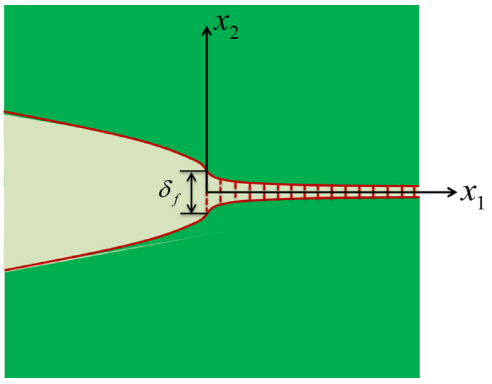

Fig. 2. Schematic of a cohesive zone ahead of a crack tip.

conservation, namely

$$\dot{\zeta} + \frac{\partial}{\partial x_1}(j_1 \delta) + (j_2^+ - j_2^-) = 0, \tag{5.4}$$

where j_2^+ and j_2^- are the solvent flux across the upper and lower interfaces of the cohesive zone at $x_2 = 0^+$ and $x_2 = 0^-$, respectively, and j_1 is the flux in the x_1 direction within the cohesive zone. For mode-I fracture, by symmetry we have $j_2^- = -j_2^+$ and $\delta = u_2^+ - u_2^- = 2u_2^+$, where u_2^+ and u_2^- are the displacements of the upper and lower interfaces. For steady state crack growth, Eq. (5.4) becomes

$$-\dot{a}\frac{\partial \zeta}{\partial x_1} + \frac{\partial}{\partial x_1}(j_1 \delta) + 2j_2^+ = 0. \tag{5.5}$$

The solvent flux in the cohesive zone is assumed to follow a linear kinetics:

$$j_1 = -M_0 \frac{\partial \mu}{\partial x_1}, \tag{5.6}$$

where the mobility constant M_0 is taken to be the same as that in the gel.

We note that the second term on the left hand side of Eq. (5.5) is generally nonlinear, which is different from the linear term in Noselli et al. (2016) assuming a constant δ.

With the solvent-permeable cohesive zone, additional energy dissipation occurs due to solvent diffusion within the cohesive zone. The modified J-integral in Eq. (3.6) is path independent only if the entire cohesive zone is enclosed within the contour C. Otherwise, for an arbitrary contour, additional terms should be included in the J-integral to account for the energy dissipation within the cohesive zone as follows:

$$J^* = \int_C \left(\hat{\phi} n_1 - \sigma_{ij} n_j \frac{\partial u_i}{\partial x_1}\right) d\Gamma + \int_A (c - c_0)\frac{\partial \mu}{\partial x_1} dA + \left(\frac{1}{2}k\delta^2 - \frac{\mu}{\Omega}\delta\right)\Big|_{x_c} + \int_0^{x_c} \frac{\delta}{\Omega}\frac{\partial \mu}{\partial x_1} dx_1, \tag{5.7}$$

where the contour C intersects the cohesive zone at $x_1 = x_c$. It can be shown that the modified J-integral in Eq. (5.7) remains path independent. In particular, by taking an infinitesimal circular contour around the crack tip with the radius $r \to 0$, we obtain

$$J_{tip}^* = J^*(r \to 0) = \left(\frac{1}{2}k\delta^2 - \frac{\mu}{\Omega}\delta\right)\Big|_{x_1 = 0}, \tag{5.8}$$

which is the crack-tip energy release rate for steady-state crack growth. For the immersed case, with $\mu_{tip} = 0$ and $\delta(x_1 = 0) = \delta_f$, we have: $J_{tip}^* = \frac{1}{2}k\delta_f^2$, which is the same as that in Noselli et al. (2016). Here, δ_f is taken to be the critical separation for fracture. As a fracture criterion, a constant δ_f implies a constant crack-tip energy release rate (J_{tip}^*), which may be considered as the *intrinsic* fracture toughness (independent of the crack speed[2]) of the gel. On the other hand, the classical J-integral (the first term on the right hand side of Eq. (5.7)) over a contour far away from the crack tip gives the remotely applied energy release rate, which is the *apparent* fracture toughness and includes energy dissipation within the contour due to solvent diffusion in the gel and in the cohesive zone. Consequently, the apparent fracture toughness is expected to be greater than the intrinsic toughness, hence poroelastic toughening (Noselli et al., 2016).

For the not-immersed case, we assume that the cohesive zone is impermeable to solvent diffusion so that the free energy density function (per unit area) is simply: $\phi_c = \frac{1}{2}k\delta^2$, and the opening stress is: $\sigma_{22} = k\delta$. Then, the modified J-integral becomes:

$$J^* = \int_C \left(\hat{\phi} n_1 - \sigma_{ij} n_j \frac{\partial u_i}{\partial x_1}\right) d\Gamma + \int_A (c - c_0)\frac{\partial \mu}{\partial x_1} dA + \left(\frac{1}{2}k\delta^2\right)\Big|_{x_c}, \tag{5.9}$$

and for a circular contour around the crack tip with $r \to 0$, we obtain

$$J_{tip}^* = J^*(r \to 0) = \frac{1}{2}k\delta_f^2, \tag{5.10}$$

where δ_f is the critical separation at the crack tip. Note that the critical separation (δ_f) could be different for the immersed and not-immersed cases, which would then lead to different intrinsic fracture toughnesses. Moreover, with no solvent diffusion in the cohesive zone for the not-immersed case, it is expected that the effect of poroelastic toughening is reduced compared to the immersed case.

With the cohesive zone model, a length scale can be defined as

$$l_c = \frac{G}{k}, \tag{5.11}$$

which characterizes the size of the cohesive zone near the crack tip although the linear elastic interaction theoretically extends to infinity. It can be shown that this length scale is similar to that for a typical cohesive zone model (Bao and Suo, 1992; Li et al., 2004): $l_c \sim \frac{G\Gamma}{\sigma_c^2}$, with a peak stress $\sigma_c = k\delta_f$ and a fracture energy $\Gamma = J_{tip}^* = \frac{1}{2}k\delta_f^2$. Here we assume $l_c \ll h$ (i.e., small-scale bridging). With this length scale, the plane-stress assumption is further limited to the cases where the specimen thickness is small compared to l_c.

By dimensional considerations, the normalized energy release rate J^*/J_e for the steady-state crack model (Fig. 1) depends on four dimensionless parameters: the applied strain ($\varepsilon_\infty = \Delta/h$), the Péclet number (Pe $= h/l_{ss}$), the Poisson's ratio (ν), and the normalized cohesive length (l_c/h), namely

$$\frac{J^*}{J_e} = \Lambda\left(\mathrm{Pe}, \varepsilon_\infty, \frac{l_c}{h}, \nu\right). \tag{5.12}$$

When $l_c/h \to 0$ (no cohesive zone), the problem becomes linear and all the fields are proportional to the applied strain ε_∞; in this case, the ratio J^*/J_e depends on two dimensionless parameters only: the Péclet number (Pe) and the Poisson's ratio (ν). The nonlinearity in the present study appears only in the poroelastic cohesive zone model for the immersed case.

We note that Wang and Hong (2012) used a cohesive zone model with nonlinear springs to calculate the crack-tip energy release rate for stationary, impermeable cracks (not-immersed) in nonlinear viscoporoelastic gels. Similarly, Yang and Lin (2018) used a linear cohesive zone model for both permeable (immersed) and impermeable (not-immersed) cracks in linear poroviscoelastic media, without considering solvent diffusion in the cohesive zone.

6. Numerical results and discussion

In this section we present numerical results obtained with a stabilized finite element method (see Appendix A) for the steady-state crack growth model in Fig. 1, first without and then with the cohesive zone. By symmetry, only half of the strip is modeled with the finite element method. A constant displacement $u_2 = h\varepsilon_\infty$ is applied at the top of the strip ($x_2 = h$), where the displacement is zero in the x_1 direction.[3] The crack face ($x_1 < 0,\ x_2 = 0$) is traction free. At the two ends of the strip ($x_1 = \pm a$), the displacement in the x_1 direction is zero and the traction in the x_2 direction is zero. The finite element mesh is similar to the previous study (Yu et al., 2018b), with quadrilateral 8**u**4p Taylor-Hood elements everywhere except for the elements around the crack tip, where the collapsed quarter-point Taylor–Hood elements (6**u**3p) are

[2] More generally, the critical separation and the intrinsic fracture toughness may depend on the crack speed due to rate-dependent fracture processes of the gel.

[3] This is different from the plane strain model in the previous study (Yu et al., 2018b), where the displacement in the x_1 direction had to be relaxed due to incompressible deformation far ahead of the crack tip.

used. With the cohesive zone model, the use of the quarter-point crack-tip elements is unnecessary, but the same mesh is used nevertheless for comparison.

To simulate a semi-infinite crack in an infinitely long strip, the half-strip model must be sufficiently long. This requires that $a \gg \max(h, l_{ss}, l_c)$. In the finite element model, we use $a \geq 10\max(h, l_{ss}, l_c)$ for all cases. With the crack tip at $x_1 = 0$, the gel at the left end ($x_1 = -a$) is fully unloaded with the chemical potential equal to the initial value, i.e., $\mu_{-\infty} = 0$. At the right end ($x_1 = a$), the gel is stretched in the x_2 direction with the strain ε_∞ while the solvent concentration remains constant ($c = c_0$), and the gel behaves as an incompressible elastic solid. Under plane stress conditions, we obtain $\mu_\infty = -2G\Omega\varepsilon_\infty$ and $\sigma_{22} = 4G\varepsilon_\infty$.[4] The chemical potentials, $\mu_{-\infty} = 0$ and $\mu_\infty = -2G\Omega\varepsilon_\infty$, are imposed at $x_1 = \pm a$ as boundary conditions. Along the top face, zero normal flux is assumed for solvent diffusion, i.e., $j_2 = 0$ at $x_2 = h$. Along the crack face ($x_1 < 0, x_2 = 0$), the chemical potential is set to be zero for the immersed case whereas the normal flux is zero ($j_2 = 0$) for the not-immersed case. On the plane ahead of the crack tip ($x_1 > 0$, $x_2 = 0$), symmetry conditions are applied if there is no cohesive zone. With the cohesive zone model, the weak form of the finite element method includes additional terms (see Eqs. A.1 and A.2 in Appendix A) for the traction-separation and solvent diffusion within the cohesive zone.

In the finite element model, all lengths are normalized by the half width ($h = 1$). The crack speed is normalized as $\dot{a}h/D_s^*$, which is equal to the Péclet number ($\mathrm{Pe} = h/l_{ss}$). The stress is normalized by the shear modulus G, the chemical potential by ΩG, and the normalized solvent concentration is Ωc.

6.1. Results without cohesive zone

Without the cohesive zone, the numerical results are compared to the asymptotic crack-tip fields in Section 4, which confirm both the angular and radial distributions of the stress, solvent concentration, and the chemical potential, similar to the previous work for steady-state crack growth under plane strain conditions (Yu et al., 2018b). The crack-tip parameters, including the stress intensity factor and the T-stress, are determined as shown in Fig. 3. Compared to the elastic solution in Eq. (3.5), the normalized stress intensity factors for both the immersed and not-immersed cases in Fig. 3a are smaller due to poroelastic shielding. Compared to the plane strain results (Yu et al., 2018b), the dependence of the stress intensity factor on the normalized crack speed is different under plane stress. At the slow crack limit ($\mathrm{Pe} \ll 1$), the stress intensity factors for both the immersed and not-immersed cases approach a constant, $K_I/(G\varepsilon_\infty\sqrt{h}) = 2\sqrt{(1+\nu)/(1-\nu)}$ (see Appendix C), which is slightly smaller than that under plane strain. As the Péclet number increases, the stress intensity factor increases monotonically for the not-immersed case but non-monotonically for the immersed case. At the fast crack limit ($\mathrm{Pe} \gg 1$), the stress intensity factor approaches another constant, $K_I/(G\varepsilon_\infty\sqrt{h}) = 4(1+\nu)/\sqrt{3}$ (Appendix B), which is greater than that under plane strain. The T-stress is negative (Fig. 3b) with a smaller magnitude compared to the plane strain results.

The angular distribution of the chemical potential in Eq. (4.7) depends on the parameter κ, which is 3 for the not-immersed case but depends on the Péclet number for the immersed case (Fig. 3c). The parameter κ governs the solvent flux across crack faces near the crack tip: when $\kappa > 3$, solvent flows into the gel; when $\kappa < 3$, solvent flows out of the gel. For the immersed case, Fig. 3c shows that $\kappa > 3$ for small Péclet numbers ($\mathrm{Pe} \leq 1$) and $\kappa < 3$ for large Péclet numbers ($\mathrm{Pe} \geq 10$) under plane stress, whereas $\kappa < 3$ for all Péclet numbers under plane strain (Yu et al., 2018b). For the not-immersed case, the chemical potential at the crack tip (μ_{tip}) depends on the Péclet number (Fig. 3d), which is negative for slow crack growth but becomes positive for fast crack growth under plane stress, whereas $\mu_{tip} > 0$ for all Péclet numbers under plane strain (Yu et al., 2018b).

For relatively fast crack growth in the immersed case, with $\mathrm{Pe} > 1$ or $l_{SS} < h$, an elastic K-field exists between the poroelastic crack-tip field and the far field. As noted in previous studies (Noselli et al., 2016; Yu et al., 2018b), at a distance away from the crack tip (roughly $r > l_{SS}$), the solvent concentration remains a constant ($c = c_0$), and the chemical potential, $\mu \sim r^{-1/2}$, is predicted by the elastic crack-tip solution (incompressible with $\nu = 0.5$). Hence, for $l_{SS} < h$, the poroelastic crack-tip field first transitions to the elastic crack-tip field and then to the homogeneous far field, as shown in Fig. 4a for different values of Pe. For each case with $\mathrm{Pe} > 1$ ($l_{SS} < h$), the elastic crack-tip field is characterized by an elastic stress intensity factor. Under plane stress conditions, the elastic crack-tip solution leads to a chemical potential:

$$\mu = -\frac{2\Omega K_e}{3\sqrt{2\pi r}}\cos\frac{\theta}{2}, \tag{6.1}$$

which is slightly different from that under plane strain conditions (Noselli et al., 2016; Yu et al., 2018b). It is found that the elastic stress intensity factor in Eq. (6.1) is identical to that for a linearly elastic strip as given in Eq. (3.5) and is independent of the crack speed ($K_e = 2G\varepsilon_\infty\sqrt{3h}$). According to Eq. (4.7) and Eq. (6.1), the chemical potential is re-scaled in Fig. 4b, where the numerical results for different Péclet numbers nearly collapse onto one curve except for the homogeneous far field ($x_1/l_{SS} > \mathrm{Pe}$). Remarkably, for a relatively large Péclet number ($\mathrm{Pe} \gg 1$), the poroelastic crack-tip solution (Eq. (4.7)) intersects with the elastic crack-tip solution (Eq. (6.1)) almost exactly at $x_1 = l_{SS}$, where the chemical potential is the lowest. As a result, the two stress intensity factors can be related approximately as:

$$K_I = \frac{2}{3}(1+\nu)K_e, \tag{6.2}$$

where $\kappa \approx 3$ is used in Eq. (4.7) for $\mathrm{Pe} \gg 1$. Hence, with $\nu < 0.5$, $K_I < K_e$ and the stress intensity factor at the crack tip is reduced by poroelastic shielding. Eq. (6.2) is confirmed numerically by a crack-tip model for the fast crack limit with $\mathrm{Pe} \gg 1$ (see Appendix B).

For relatively slow crack growth, with $\mathrm{Pe} < 1$ or $l_{SS} > h$, the elastic crack-tip field does not exist and a different transition from the poroelastic crack-tip field to the homogeneous far field is observed in Fig. 5. In this case, the chemical potential follows the poroelastic crack-tip solution up to approximately $x_1 = h$ and becomes a constant for $x_1 > l_{SS}$. In between ($h < x_1 < l_{SS}$), the magnitude of the chemical potential increases almost linearly (i.e., $\mu \sim r$). Such a transition can be predicted by a one-dimensional (1D) diffusion model for both the immersed and not-immersed cases (see Appendix C), which is essentially the same as the results in the previous study under plane strain conditions (Yu et al., 2018b). As shown in Fig. 5, the chemical potential and the opening stress ahead of the crack tip ($x_1 > h$) are well predicted by the 1D model for the cases with $\mathrm{Pe} < 1$.

Without a cohesive zone, the crack-tip energy release rate for steady state crack growth can be calculated by the modified J-integral in Eq. (3.6) or by Eq. (4.9) with the stress intensity factors in Fig. 3a. As in previous studies (Bouklas et al., 2015; Yu et al., 2018b), the domain integral method is implemented to calculate the modified J-integral as a function of the Péclet number. As shown in Fig. 6, the trend is similar to the stress intensity factor in Fig. 3a. At the slow crack limit ($\mathrm{Pe} \ll 1$), the energy release rate approaches a constant, $J^*/J_e = \frac{1}{2(1-\nu)}$ (Appendix C), for both the immersed and not-immersed cases, which is exactly the same as for plane strain (although the corresponding stress intensity factors are slightly different). At the fast crack limit ($\mathrm{Pe} \gg 1$), the energy release rate approaches another constant, $J^*/J_e = 2(1+\nu)/3$ (Appendix B), which is larger than that for plane strain. The larger J^*/J_e suggests that the poroelastic shielding is weaker under plane stress conditions.

[4] With the cohesive zone model, the chemical potential at $x_1 = a$ is slightly different and depends on l_c/h for both immersed and not-immersed cases. This effect however is negligible when $l_c/h \ll 1$ (small-scale bridging).

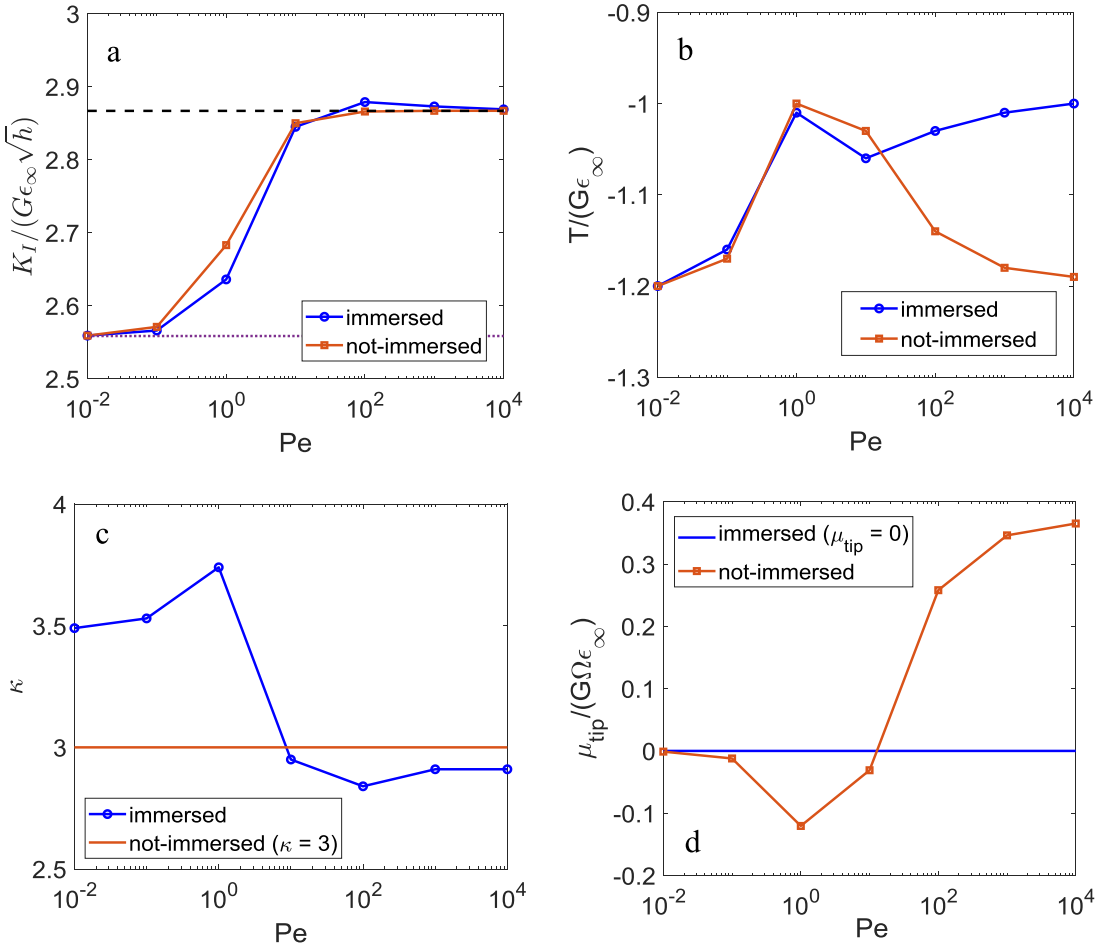

Fig. 3. Numerically determined crack-tip parameters versus the Péclet number (Pe = $\dot{a}h/D_s^*$) with $\nu = 0.2414$: (a) normalized stress intensity factor (with dotted and dashed lines for the slow and fast crack limits, respectively); (b) normalized T-stress; (c) κ parameter; (d) normalized chemical potential at the crack tip.

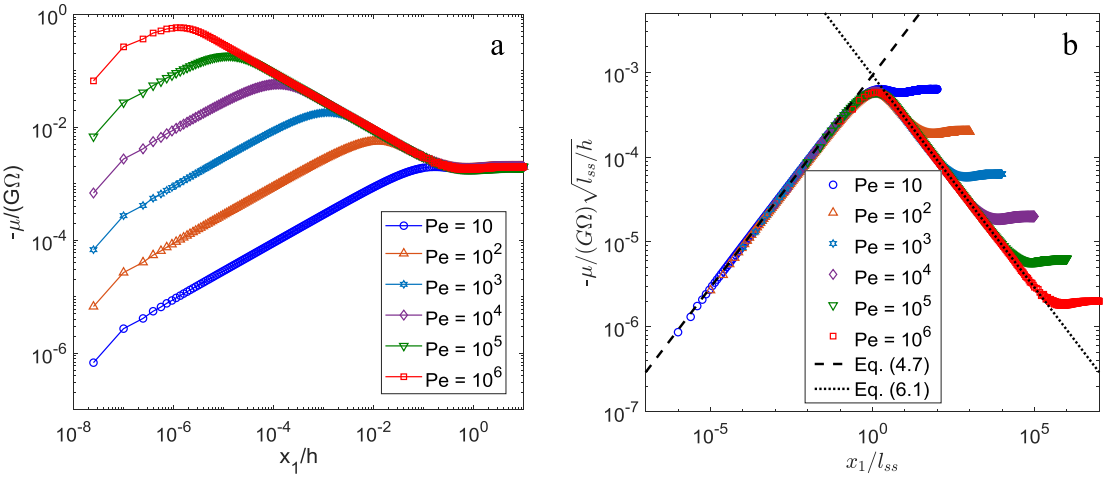

Fig. 4. Chemical potential on the plane ahead of the crack tip for different Péclet numbers (Pe > 1), for immersed cases with $\nu = 0.2414$.

6.2. Results with a cohesive zone

With the cohesive zone model in Section 5, the finite element method is slightly modified to account for the traction-separation and solvent diffusion in the cohesive zone (Appendix A). Here, we first present the numerical results for the case of small-scale bridging with a relatively small cohesive length ($l_c/h = 10^{-5}$) and then discuss the effect of the cohesive length scale.

Fig. 7 plots the angular distributions of the stress and solvent concentration at two different radii around the crack tip for the immersed case with Pe = 10 and $\varepsilon_\infty = 0.001$. At a radial distance $r/h = 10^{-3}$, about two orders of magnitude larger than the cohesive zone length scale ($l_c/h = 10^{-5}$) yet small in comparison to the specimen size, the numerical results agree well with the asymptotic crack-tip solution in Section 4. However, at a radial distance smaller than the cohesive zone length scale, $r/h = 10^{-6}$, the angular distributions differ markedly from the asymptotic solution. For this particular case, the cohesive zone ($r \le l_c$) near the crack tip is enclosed by the poroelastic

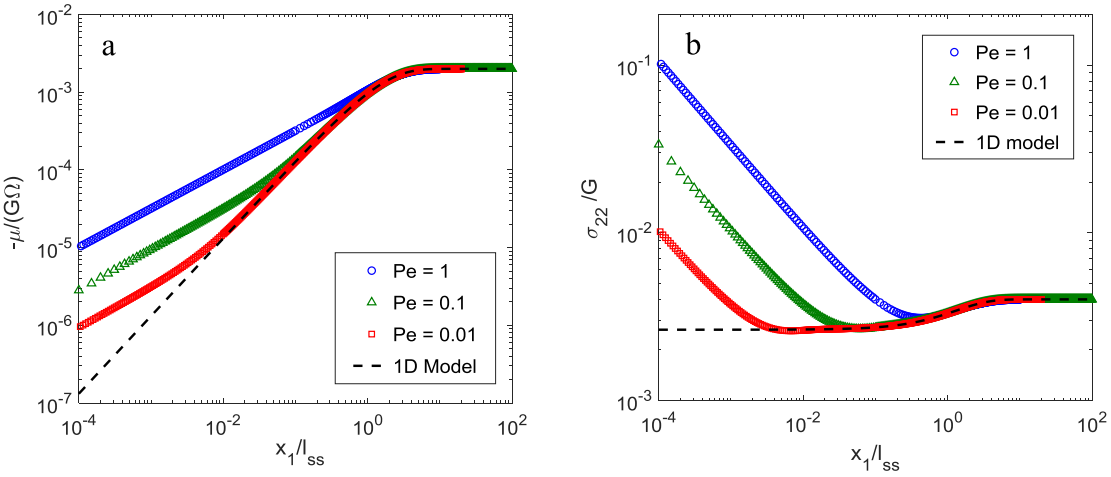

Fig. 5. (a) Chemical potential and (b) opening stress ahead of the crack tip for relatively slow crack growth (Pe $\leq$ 1) with $\nu = 0.2414$.

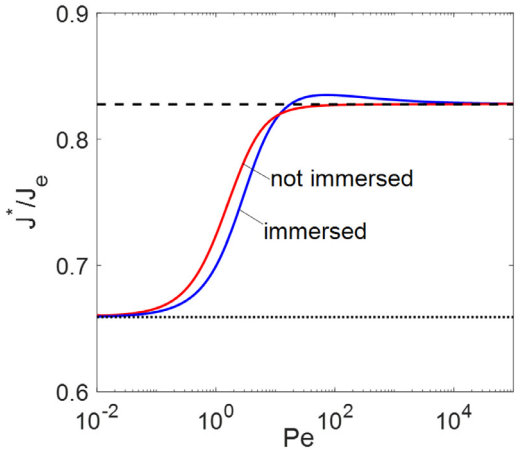

Fig. 6. Normalized energy release rate as a function of the Péclet number with $\nu = 0.2414$ (dotted and dashed lines for the slow and fast crack limits, respectively).

zone ($r \leq l_{ss}$), and the poroelastic crack-tip solution prevails in the annular region $l_c < r < l_{ss}$. Closer to the crack tip ($r \leq l_c$), the results are influenced by the cohesive zone with reduced stress and solvent concentration. Farther away ($r > l_{ss}$), the poroelastic crack-tip field transitions to the elastic K-field and then to the far field, similar to that shown in Fig. 4. Fig. 8a shows the crack opening displacement including the opening in the cohesive zone ($x_1 > 0,\ x_2 = 0$). With the cohesive zone model, the crack opening is larger than the prediction by the asymptotic solution in Eq. (4.5). *Re*-plotting the crack opening behind the crack tip ($x_1 < 0$) on a log-log scale (Fig. 8b) shows clearly a transition from the asymptotic solution in the annulus ($l_c < r < l_{ss}$) to the solution influenced by the cohesive zone near the crack tip ($r \leq l_c$). A similar transition is seen for the opening stress and chemical potential ahead of the crack tip in Figs. 8 (c-d). In particular, Fig. 8c shows that, with the cohesive zone, the stress near the crack tip ($r \to 0$) is reduced and not singular.

With the cohesive zone model, the crack-tip energy release rate can be calculated directly by Eq. (5.8) or (5.10) with $J^*_{tip} = \frac{1}{2}k\delta_f^2$ for both the immersed and not-immersed cases, where the crack-tip opening (δ_f) depends on the applied strain (ε_∞) nonlinearly for the immersed case but linearly for the not-immersed case. Fig. 9 shows the normalized energy release rate as a function of the Péclet number with $\varepsilon_\infty = 10^{-3}$. Compared to Fig. 6, the presence of a small-scale cohesive zone ($l_c/h = 10^{-5}$) has no effect on the energy release rate for relatively slow crack growth with Pe < 100. In this case, $l_c \ll l_{ss}$, and the cohesive zone is largely enclosed by the diffusion zone. For fast crack growth (Pe > 100), however, the diffusion zone size (l_{ss}) becomes comparable to or even smaller than the cohesive length scale (l_c), and the poroelastic effect is influenced by the cohesive zone. For the immersed case, the crack-tip energy release rate decreases as the Péclet number increases, whereas the trend is opposite for the not-immersed case.

For very fast crack growth (Pe $> 10^5$), the diffusion length is smaller than the cohesive length ($l_{ss} < l_c \ll h$). In this case, a very fine mesh is required at the crack tip to resolve both length scales. Alternatively, for the immersed case, a crack tip model can be used with the elastic K-field imposed as the remote boundary condition, similar to the crack-tip model without the cohesive zone (Appendix B). With the poroelastic cohesive zone model, however, the problem becomes nonlinear. By dimensional considerations, the normalized energy release rate in the crack-tip model is a function of three dimensionless groups:

$$\frac{J^*}{J_e} = f\left(\frac{K_e}{G\sqrt{l_c}}, \frac{l_c}{l_{ss}}, \nu\right). \tag{6.3}$$

To be consistent with the long strip model, the same parameters, $l_c/h = 10^{-5}$, $\nu = 0.2414$ and $K_e = 2G\varepsilon_\infty\sqrt{3h}$, are used in the crack-tip model. As a result, the dimensionless loading parameter is: $\frac{K_e}{G\sqrt{l_c}} = 200\sqrt{30}\varepsilon_\infty$, which is 1.095 for $\varepsilon_\infty = 0.001$. Correspondingly, the Péclet number is related to the ratio of the two length scales as: $\frac{l_c}{l_{ss}} = 10^{-5}$Pe. Note that, without the cohesive zone, the normalized energy release rate from the crack-tip model (Appendix B) depends only on Poisson's ratio (Eq. B.3).

In the finite element simulations for the crack tip model, we set $l_c = 1$ to normalize all the lengths, while the diffusion length (l_{ss}) is varied for different crack speeds ($\dot{a}$). The radius of the semicircular domain is chosen to be much larger than both l_c and l_{ss}, i.e., $r \geq 10\max(l_c, l_{ss})$. The normalized energy release rate obtained from the crack-tip model is plotted as a function of l_c/l_{ss} in Fig. 10a. For $l_c/l_{ss} \ll 1$, the normalized energy release rate approaches the fast crack limit (Pe $\gg 1$) without the cohesive zone; in this case, the presence of the cohesive zone has negligible effect. On the other hand, as l_c/l_{ss} increases, the normalized energy release rate decreases and approaches zero when $l_c/l_{ss} \gg 1$. Qualitatively similar results were obtained by Noselli et al. (2016) using a linear poroelastic cohesive zone model.

The results from the crack-tip model can be compared to that for the long strip model with the relation: $l_c/l_{ss} = 10^{-5}$Pe for $l_c/h = 10^{-5}$, which extends the range of the Péclet number up to 10^{10} as shown in Fig. 10b. Apparently, for relatively fast crack growth (Pe > 100), the crack-tip energy release rate decreases with increasing crack speed under the same applied strain ($\varepsilon_\infty = 0.001$). This can be understood as a result of the poroelastic cohesive zone model for the immersed case, where

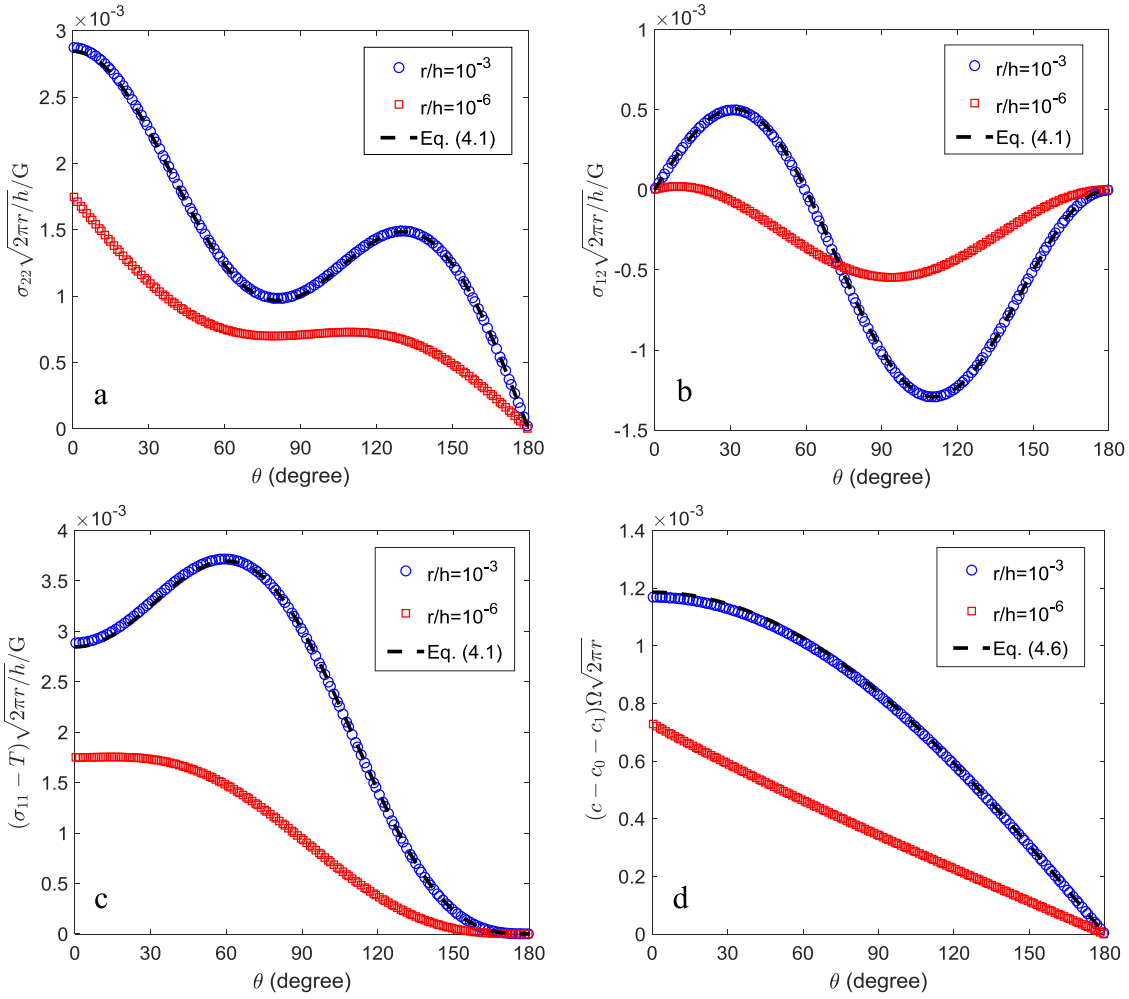

Fig. 7. Angular distributions of the stress components (a-c) and solvent concentration (d) for the immersed case with the nonlinear poroelastic cohesive zone model (Pe = 10, $\varepsilon_\infty = 0.001$, $\nu = 0.2414$, $l_c/h = 10^{-5}$).

solvent diffusion within the cohesive zone dissipates additional energy. By Eq. (5.7), with a contour far away from the crack tip, the third term on the right-hand side is negligible and the fourth term accounts for the energy dissipation within the cohesive zone. It is found that, with increasing Péclet number, the opening separation in the cohesive zone decreases under the same applied strain (Fig. 11a), but the magnitude of the chemical potential and its gradient ($\partial\mu/\partial x_1$) in the cohesive zone increase more significantly, leading to more energy dissipation. The opening separation in the cohesive zone is related to the solvent concentration by Eq. (5.3) and thus constrained by the kinetics of solvent diffusion when the crack speed is high. In particular, the crack-tip opening decreases with increasing crack speed under the same applied strain for the immersed case (Fig. 11a).

For the not-immersed case, with no solvent diffusion in the cohesive zone, the numerical results show the opposite trend for the crack-tip energy release rate (Fig. 9) and the opening displacement (Fig. 11b). Evidently, as the Péclet number increases, the effect of poroelastic shielding decreases in the not-immersed case, leading to a larger crack-tip energy release rate and a larger crack-tip opening. Here, solvent diffusion is restricted to a small region near the crack tip, where the presence of a cohesive zone reduces solvent concentration and associated energy dissipation. In the limiting case of very fast crack growth with Pe $\gg 1$ or $l_{ss} \ll l_c$, the energy dissipation by solvent diffusion vanishes and the crack-tip energy release rate approaches the elastic limit ($J^*/J_e \to 1$) as shown in Fig. 9.

In general, for both the immersed and not-immersed cases, the normalized crack-tip energy release rate for steady state crack growth in the long strip model can be written as a function of four parameters in Eq. (5.12). With the nonlinear poroelastic cohesive zone model for the immersed case, the normalized energy release rate depends on the applied strain as shown in Fig. 12, where the ratio J^*/J_e increases with the applied strain for fast crack growth (e.g., Pe = 10^6) but is nearly a constant for relatively slow crack growth (e.g., Pe = 10^2). As noted earlier, the presence of a small-scale cohesive zone ($l_c/h = 10^{-5}$) has negligible effect on slow crack growth. For the not-immersed case, with a linear cohesive zone model (no solvent diffusion), the ratio J^*/J_e is independent of the applied strain.

The effect of the cohesive length scale on the normalized crack-tip energy release rate is shown in Fig. 13. Under the condition of small-scale bridging ($l_c/h \ll 1$), the normalized energy release rate decreases with increasing cohesive length for the immersed case due to increasing energy dissipation by solvent diffusion in the permeable cohesive zone. On the other hand, with no solvent diffusion in the cohesive zone for the not-immersed case, the energy release rate increases and approaches the elastic limit ($J^*/J_e \to 1$) for fast crack growth (Pe = 10^5 and 10^6). When $l_c/h > 10^{-2}$, the trend starts to change in both cases. For the immersed case, the normalized energy release rates for fast crack growth (Pe = 10^5 and 10^6) start increasing, possibly due to reduced energy dissipation by solvent diffusion in the bulk of the gel. In contrast, the normalized energy release rate decreases with increasing l_c/h ($> 10^{-2}$) for the not-immersed case, which is a result of effectively reduced stiffness due to the elastic cohesive zone. Far ahead of the crack

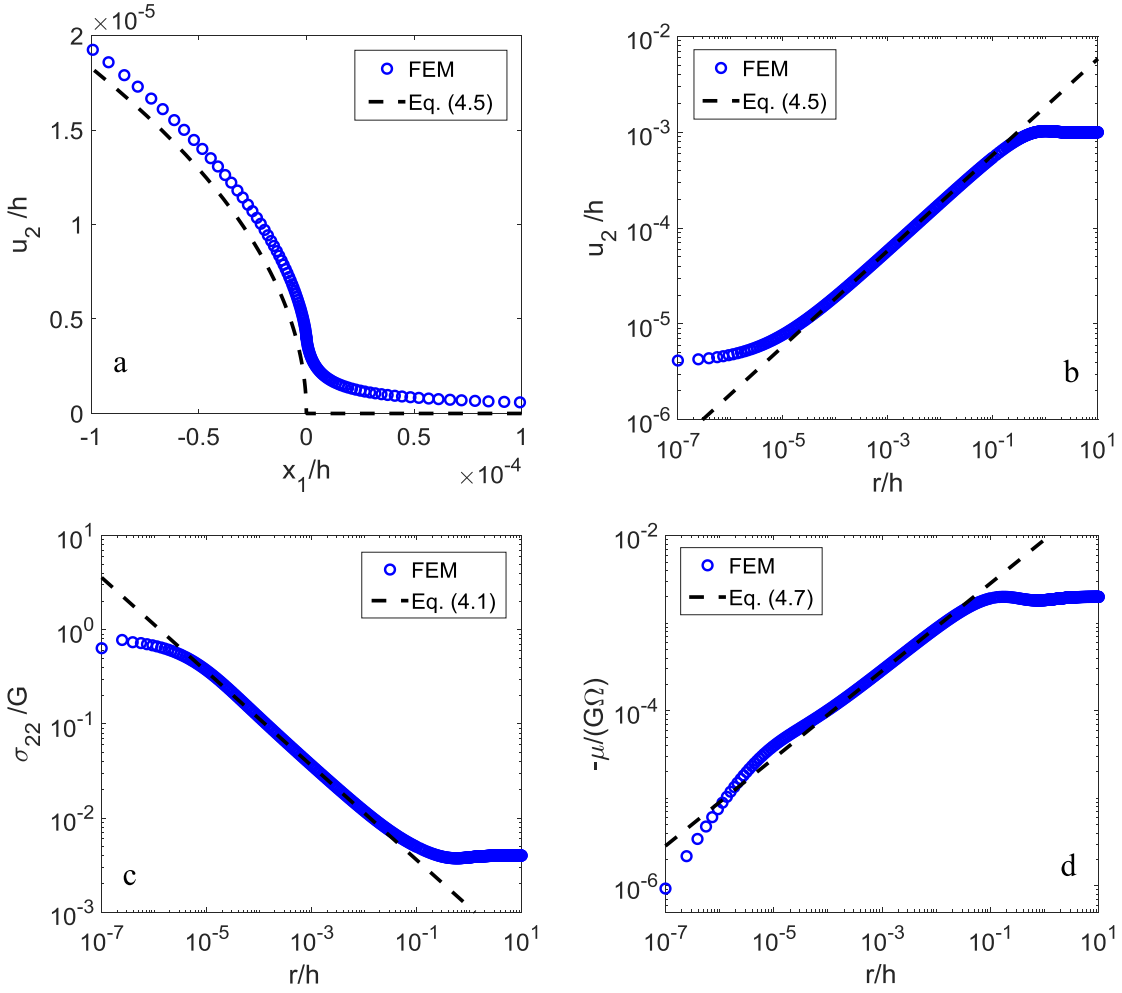

Fig. 8. (a) and (b): Opening displacement in linear and log-log scales; (c) and (d): opening stress and chemical potential straight ahead of the crack tip, for the immersed case with the poroelastic cohesive zone model (Pe = 10, $\varepsilon_\infty = 0.001$, $\nu = 0.2414$, $l_c/h = 10^{-5}$).

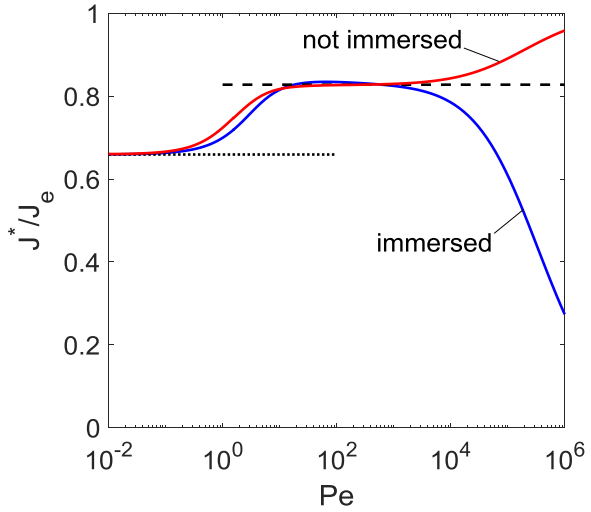

Fig. 9. Normalized crack-tip energy release rates as functions of the Péclet number for the immersed and not-immersed cases with the cohesive zone model ($\varepsilon_\infty = 0.001$, $l_c/h = 10^{-5}$, and $\nu = 0.2414$). The dotted and dashed lines are for the slow and fast crack limits without the cohesive zone.

tip, with the elastic cohesive zone, the opening stress is related to the applied strain by:

$$\sigma_{22} = \frac{4G\varepsilon_\infty}{\left(1 + \frac{2l_c}{h}\right)}. \tag{6.4}$$

With the reduced stiffness, the remotely applied energy release rate is also reduced:

$$J_a = \frac{J_e}{\left(1 + \frac{2l_c}{h}\right)}. \tag{6.5}$$

As shown in Fig. 13b, the numerical results for J^*/J_e converge onto J_a/J_e for the not-immersed cases, indicating negligible energy dissipation by solvent diffusion (independent of the crack speed for $l_c/h > 10^{-1}$).

6.3. Discussion

Without the cohesive zone model, the condition for steady state crack growth at a particular crack speed may be established by setting the crack-tip energy release rate equal to an intrinsic steady-state fracture toughness, i.e., $J^* = \Gamma_{ss}$, where the intrinsic toughness may also be a function of the crack speed as a result of rate-dependent fracture processes (Long and Hui, 2016). Using the long-strip pure-shear specimen, the steady-state crack speed $\dot{a}$ can be measured as a function of the applied strain ε_∞. Then, by Eq. (5.12), the intrinsic steady-state toughness can be determined as a function of the crack speed as

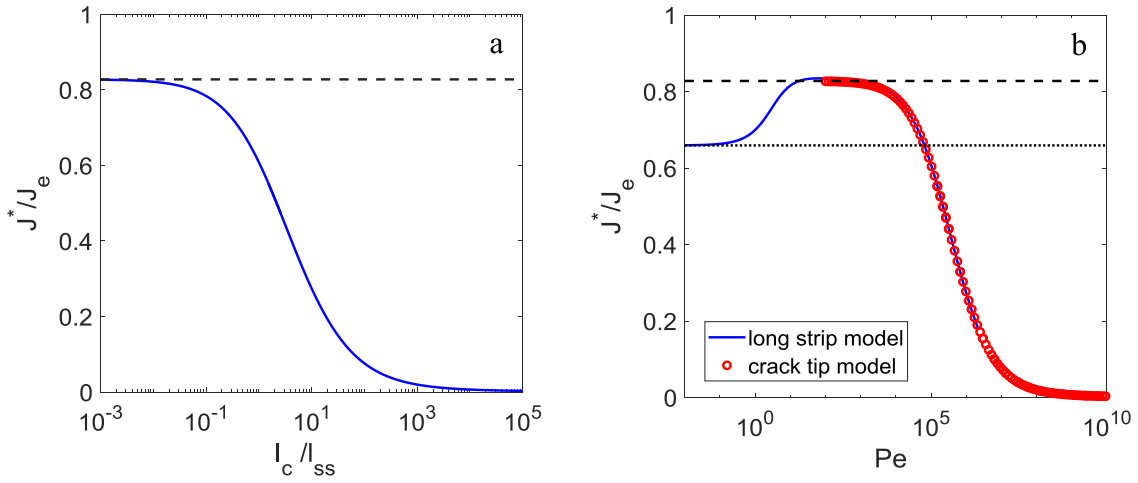

Fig. 10. (a) Normalized energy release rate from the crack-tip model ($\frac{K_e}{G\sqrt{l_c}} = 1.095$, $\nu = 0.2414$); (b) Comparison of the crack-tip model and the long strip model for the immersed case with a poroelastic cohesive zone ($l_c/h = 10^{-5}$). The dotted and dashed lines are for the slow and fast crack limits without the cohesive zone.

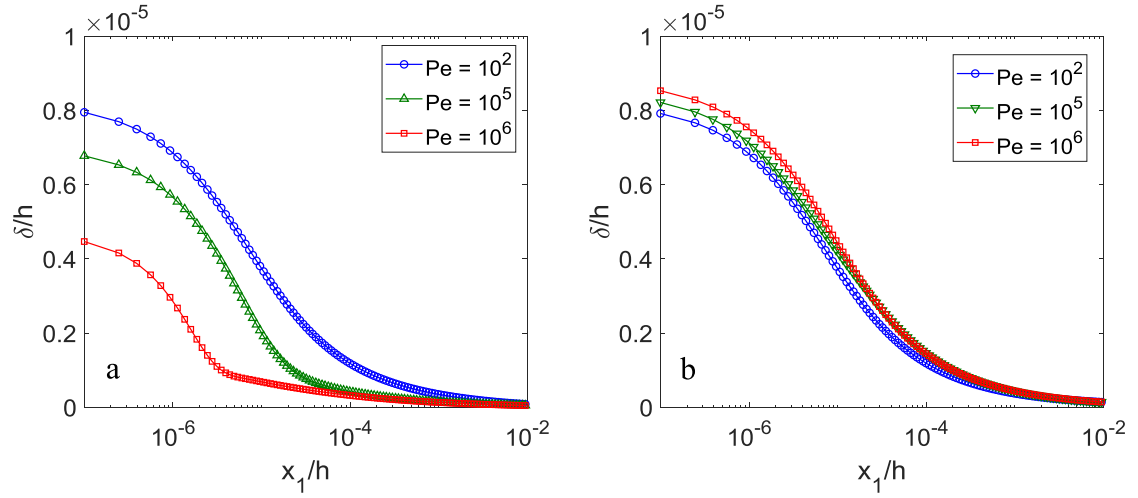

Fig. 11. The opening displacement in the cohesive zone with increasing crack speed under the same applied strain ($\varepsilon_\infty = 0.001$, $l_c/h = 10^{-5}$, $\nu = 0.2414$): (a) for the immersed case and (b) for the not-immersed case.

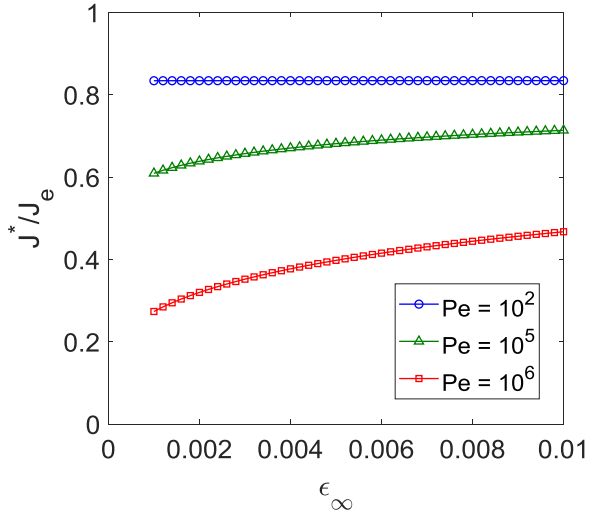

Fig. 12. Normalized crack-tip energy release rates as functions of the applied strain for the immersed case ($l_c/h = 10^{-5}$, $\nu = 0.2414$).

$$\Gamma_{ss}(\dot{a}) = J_e \Lambda(\mathrm{Pe},\nu), \tag{6.6}$$

where $J_e = 4G\varepsilon_\infty^2 h$ and the function $\Lambda(\mathrm{Pe}, \nu)$ can be calculated as shown in Fig. 6 for $\nu = 0.2414$. Typically, without considering the poroelastic effect, J_e is reported as the fracture toughness, which is greater than the intrinsic toughness. Moreover, Eq. (6.6) implies that the apparent toughness J_e would generally depend on the specimen size through the Péclet number ($\mathrm{Pe} = \dot{a}h/D_s^*$) whereas the intrinsic toughness Γ_{ss} should be independent of the specimen size.

With the cohesive zone model (Section 4), the crack-tip energy release rate for steady state crack growth is related to the opening displacement at the crack tip: $J_{tip}^* = \frac{1}{2}k\delta_f^2$, which implies an intrinsic steady-state fracture toughness: $\Gamma_{ss} = \frac{1}{2}k\delta_f^2$. To measure the intrinsic toughness, in addition to the crack speed and the applied strain, another parameter must be determined due to the cohesive zone: l_c/h. For example, the crack-tip opening displacement may be measured as a function of the crack speed, $\delta_f(\dot{a})$, which can be related to the applied strain and the cohesive length scale as:

$$\delta_f(\dot{a}) = 2h\varepsilon_\infty \cdot g\left(\mathrm{Pe},\varepsilon_\infty, \frac{l_c}{h}, \nu\right), \tag{6.7}$$

where $g(\mathrm{Pe},\varepsilon_\infty, \frac{l_c}{h}, \nu)$ is a dimensionless function as shown in Fig. 14. Under a given applied strain, the crack-tip opening increases with increasing cohesive length. For the immersed case, the normalized crack-

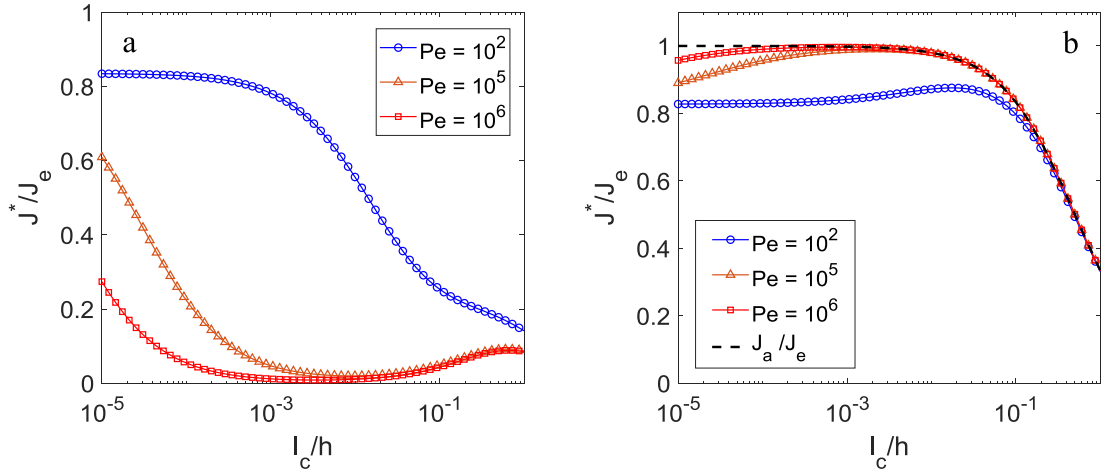

Fig. 13. Normalized crack-tip energy release rate as a function of the cohesive length scale (l_c/h) for the (a) immersed and (b) not-immersed cases ($\varepsilon_\infty = 0.001,\ \nu = 0.2414$).

tip opening depends on the Péclet number and the applied strain due to the nonlinear poroelastic cohesive zone model. For the not-immersed case with a linear elastic cohesive zone model, the normalized crack-tip opening is independent of the applied strain, and interestingly, it appears to be insensitive to the Péclet number (Fig. 14b). In either case, the cohesive length (l_c/h) can be determined from the measured crack-tip opening displacement the along with the crack speed and the applied strain. Then, the intrinsic toughness can be obtained by Eq. (5.12) as:

$$\Gamma_{ss}(\dot{a}) = J_e \Lambda\left(\mathrm{Pe}, \varepsilon_\infty, \frac{l_c}{h}, \nu\right), \tag{6.8}$$

where the dimensionless function $\Lambda(\mathrm{Pe}, \varepsilon_\infty, \frac{l_c}{h}, \nu)$ can be calculated as shown in Fig. 9.

If the intrinsic fracture toughness (Γ_{ss}) is known for the gel, Eq. (6.6) or (6.8) may be used to predict the steady-state crack speed in a long strip pure-shear specimen subject to an applied strain ε_∞. Further, if Γ_{ss} is a constant independent of the crack speed, the results in Fig. 6 (without a cohesive zone) suggest that the crack growth is unstable in the not-immersed case because the crack-tip energy release rate increases with increasing crack speed. In the immersed case, stable growth is possible for fast crack speeds (Pe > 100) when the crack-tip energy release rate decreases slightly with increasing crack speed. With the cohesive zone model, the numerical results in Fig. 9 suggest that the crack growth remains unstable for the not-immersed case unless the intrinsic fracture toughness (Γ_{ss}) increases with increasing crack speed. For the immersed case, however, significant poroelastic toughening is predicted and the crack growth is stable for Pe > 100. As shown in Fig. 15a, the crack-tip energy release rate increases as the applied strain increases at each crack speed. Assuming a constant Γ_{ss} (e.g., $\Gamma_{ss} = 10^{-4}Gh$), the applied strain required for the steady-state crack growth at each speed can be determined by setting $J^* = \Gamma_{ss}$. Fig. 15b shows the applied energy release rate ($J_e = 4G\varepsilon_\infty^2 h$) thus obtained as a function of the crack speed. Evidently, for the immersed case, the effect of poroelastic toughening increases with increasing crack speed ("velocity toughening"). A similar effect was predicted by Noselli et al. (2016) in terms of the applied stress intensity factor in a crack-tip model, where the toughening ratio (J_e/Γ_{ss} or K_e/K_{ss}) is relatively small. Experimentally, Lefranc and Bouchaud (2014) found that the measured energy release rate increased significantly with increasing crack speed in agar gels, which may include effects from both poroelastic toughening and rate-dependent intrinsic toughness.

To further understand the effect of poroelastic toughening associated with the solvent-permeable cohesive zone model for the immersed case, we show in Fig. 16 (a-c) the opening displacement, the opening stress, and the chemical potential in the cohesive zone ahead of the crack tip at different crack speeds, corresponding to the same intrinsic toughness ($\Gamma_{ss} = 10^{-4}Gh$). Remarkably, the numerical results suggest a rate-dependent traction-separation relation as shown in Fig. 16d. For relatively slow crack growth (Pe = 100), the chemical potential in the cohesive zone is small and the traction-separation

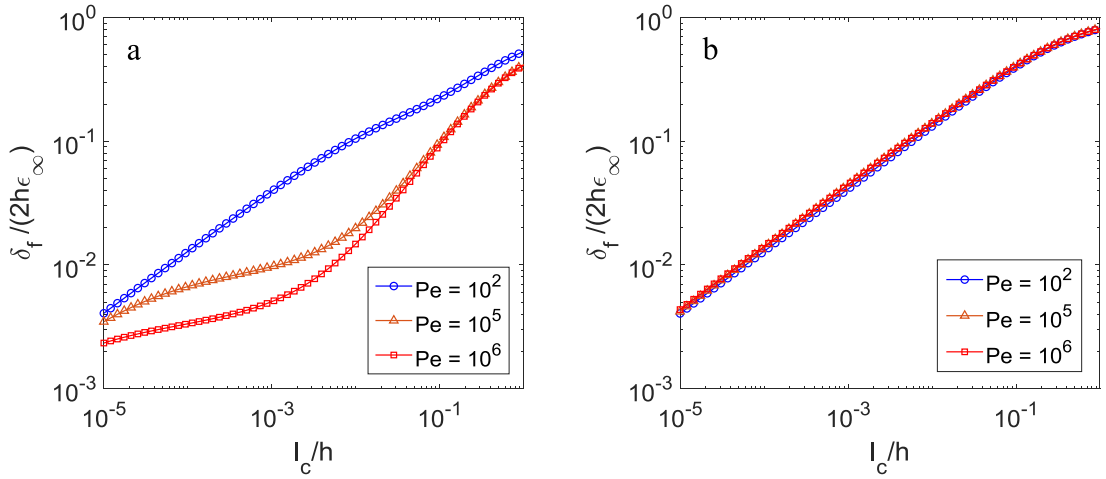

Fig. 14. Normalized crack-tip opening as a function of the cohesive length scale (l_c/h) for the (a) immersed and (b) not-immersed cases ($\varepsilon_\infty = 0.001,\ \nu = 0.2414$).

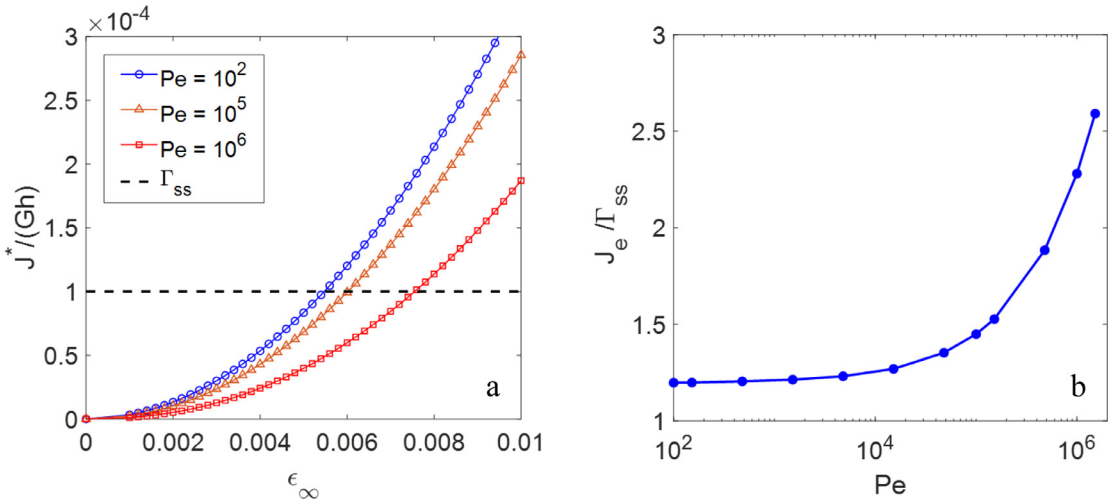

Fig. 15. (a) The crack-tip energy release rate versus the applied strain for the immersed case with $l_c/h = 10^{-5}$ and $\nu = 0.2414$. (b) The applied energy release rate ($J_e = 4G\varepsilon_\infty^2 h$) as a function of the Péclet number for $\Gamma_{ss} = 10^{-4}Gh$.

relation is linear ($\sigma_{22} \approx k\delta$). As the crack speed increases, the magnitude of chemical potential increases and adds significantly (as a negative pore pressure) onto the opening stress following Eq. (5.2). As a result, the traction-separation relation becomes nonlinear and dependent on the crack speed. For very fast crack growth (Pe = 10^6), the opening stress reaches a peak ahead of the crack tip where the chemical potential is the lowest. Correspondingly, the traction-separation relation becomes non-monotonic with apparent softening after the peak. With the same intrinsic toughness ($\Gamma_{ss} = 10^{-4}Gh$ and $l_c/h = 10^{-5}$), the opening displacement and stress at the crack tip ($x_1 = 0$) are

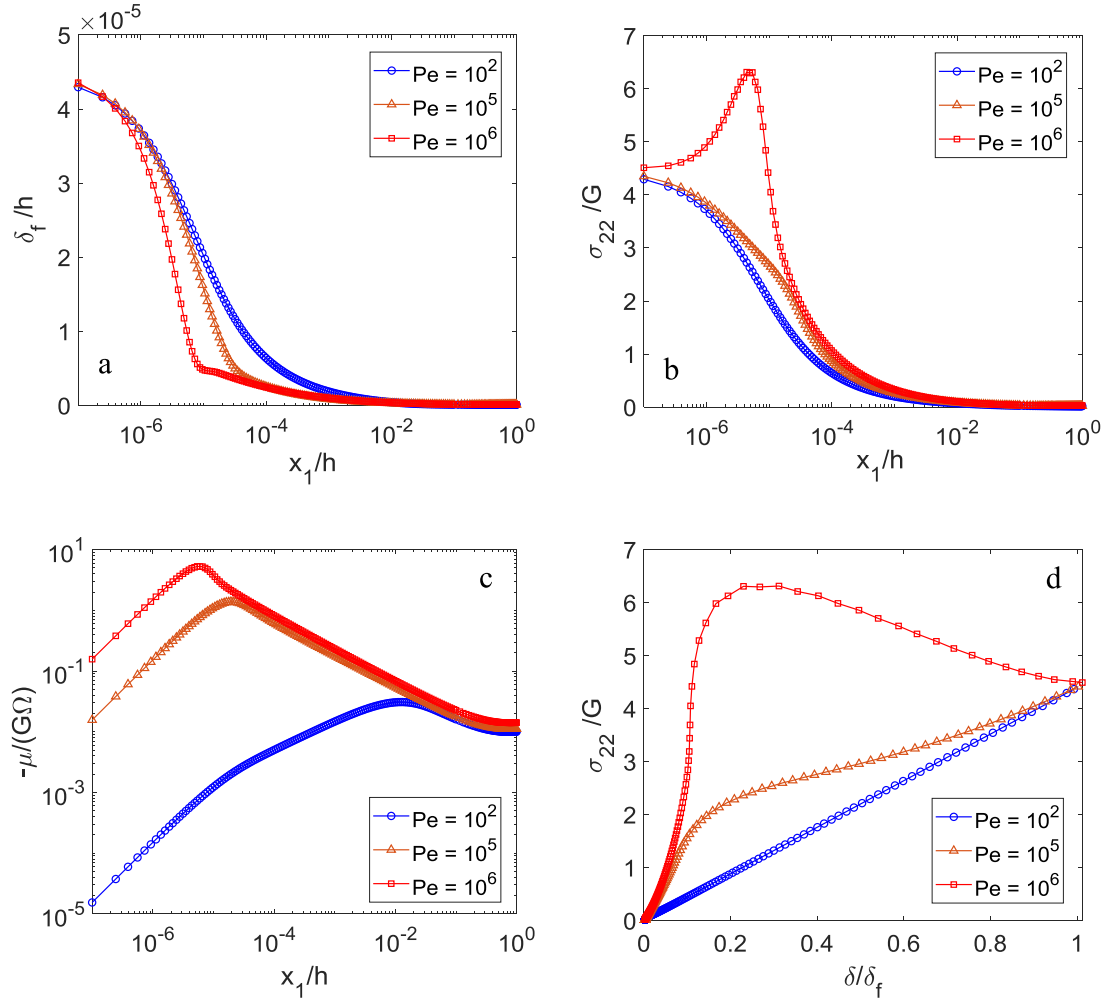

Fig. 16. (a) Opening displacement, (b) opening stress, and (c) chemical potential in the solvent-permeable cohesive zone at different crack speeds for the immersed case with $\Gamma_{ss} = 10^{-4}Gh$ and $l_c/h = 10^{-5}$. (d) Corresponding steady-state traction-separation relations at different crack speeds.

independent of the crack speed, but the trajectory of the traction-separation relation depends on the fracture process including the effect of chemical potential and solvent diffusion within the cohesive zone. Interestingly, by integrating the traction-separation relation we would obtain a rate-dependent fracture energy that includes not only the intrinsic toughness but also the poroelastic contribution due to the solvent-permeable cohesive zone; while the former is assumed to be independent of crack speed here, the latter is inherently rate dependent. We note that, despite the small-scale bridging condition ($l_c/h = 10^{-5}$), the effect of the poroelastic cohesive zone is significant when the diffusion length ($l_{ss}/h = 1/\mathrm{Pe}$) is equally small or even smaller in the case of fast crack growth ($\mathrm{Pe} \gg 1$).

Finally, to put the theoretical results into physical perspective, we estimate the Péclet numbers in typical experiments. Taking D_s^* to be 10^{-11} m^2/s and assuming h to be on the order of 10 mm, for crack speeds ranging from 0.001 to 10 mm/s (Lefranc and Bouchaud, 2014), the Péclet numbers are in the range of 10^3 to 10^7. However, the value of D_s^* could vary significantly for different gels.

7. Concluding remarks

Based on a linear poroelastic formulation, we present a theoretical and numerical study on steady-state crack growth in polymer gels under plane stress conditions, including the asymptotic crack-tip fields and a nonlinear poroelastic cohesive zone model. A stabilized finite element method was implemented to simulate steady-state crack growth in long strip pure-shear specimens. It is found that, without the cohesive zone model, the normalized crack-tip energy release rate at the fast crack limit is greater than the slow crack limit, suggesting reduced poroelastic toughening for fast crack growth under plane stress conditions, while the two limits are identical under plane strain conditions in a previous study (Yu et al., 2018b). With a solvent-permeable cohesive zone for the case of immersed specimens, solvent diffusion within the cohesive zone enhances the poroelastic toughening significantly as the crack speed increases, leading to rate-dependent traction-separation relations. On the other hand, with no solvent diffusion in the cohesive zone for the not-immersed case, the poroelastic effect diminishes as the crack speed increases. Based on the present study, the intrinsic steady-state toughness of a poroelastic gel can be determined as a function of the crack speed using long-strip pure-shear specimens by measuring the crack speed and the applied strain as well as the crack-tip opening.

It should be noted that the linear poroelastic analysis is limited to the cases where large deformation of the gel is confined within a small region around the crack tip, similar to the small-scaling yielding condition for the linear elastic fracture mechanics. Such cases may be found in many brittle gels with fracture toughness less than ~10 J/m^2 (e.g., Lefranc and Bouchaud, 2014). For gels with higher toughness, we expect qualitatively similar effects from poroelasticity in terms of rate-dependent toughening due to solvent diffusion, but quantitatively different due to the nonlinear coupling between large deformation and solvent diffusion (similar to large-scale yielding). Specifically, the asymptotic crack-tip fields would be different and analytically intractable, the modified J-integral can be readily extended to the nonlinear cases (Bouklas et al., 2015), and similar cohesive zone models can be adopted to study crack growth with large deformation and nonlinear fracture processes.

Declaration of Competing Interest

The authors declare that they have no known competing financial interests or personal relationships that could have appeared to influence the work reported in this paper.

Acknowledgements

The authors gratefully acknowledge financial support of this work by National Science Foundation through Grant No. CMMI-1538658.

Supplementary materials

Supplementary material associated with this article can be found, in the online version, at doi:10.1016/j.mechmat.2020.103320.

Appendix A: Formulation of a Stabilized Finite Element Method

The solution to the steady-state boundary value problem as described in Section 3 consists of a vector field of displacements and a scalar field of chemical potential, $\mathbf{u}(\mathbf{x})$ and $\mu(\mathbf{x})$. Similar to the previous work (Yu et al., 2018b), the weak form of Eqs. (2.4) and (2.5) (replacing $\partial c/\partial t$ with $-\dot{a}\partial c/\partial x_1$ for the steady state) is obtained by using the test functions $\tilde{\mathbf{u}}(\mathbf{x})$ and $\tilde{\mu}(\mathbf{x})$ with the divergence theorem, namely

$$\int_{A_0} \sigma_{ij}\tilde{u}_{i,j}dA + \int_0^a \left(2ku_2 - \frac{\mu}{\Omega}\right)\tilde{u}_2 dx = \int_{C_0} \tau_i \tilde{u}_i d\Gamma, \tag{A.1}$$

$$\int_{A_0} \left(c\delta_{1k} - \tfrac{1}{\dot{a}}j_k\right)\tilde{\mu}_{,k}dA - \sum \int_{\Omega^e} \left(-\dot{a}\tfrac{\partial c}{\partial x_1} + \tfrac{\partial j_k}{\partial x_k}\right)\tau^e\tilde{\mu}_1 dA + \tfrac{1}{\Omega\dot{a}}\int_0^a \left(\dot{a}u_2 + \Omega M_0 u_2 \tfrac{\partial \mu}{\partial x_1}\right)\tilde{\mu}_1 dx = \int_{C_0} \left(cn_1 + \tfrac{i}{\dot{a}}\right)\tilde{\mu} d\Gamma, \tag{A.2}$$

where the second term of Eq. (A.2) is for the consistent streamline-upwind-Petrov-Galerkin (SUPG) stabilization (Brooks and Hughes, 1982; Franca et al., 2006). The second term of Eq. (A.1) and the third term of Eq. (A.2) account for the cohesive zone (for the immersed case only) ahead of the crack tip. For the not-immersed case with an impermeable cohesive zone, the second term of Eq. (A.1) is simpler (with $2ku_2$ in the bracket) and the third term of Eq. (A.2) is not needed. Without a cohesive zone, both terms are dropped.

Similar to our previous studies (Yu et al., 2018a & 2018b), the 8**u**4p Taylor-Hood elements with biquadratic serendipity interpolation for displacement and bilinear interpolation for chemical potential are used to alleviate numerical oscillations. Upon discretization, the weak form in Eqs. (A.1) and (A.2) leads to a system of nonlinear equations for the immersed case, which are solved numerically by the standard Newton-Raphson method. For the not-immersed case, a system of linear equations are obtained and solved by using an open-source package PETSc (Balay et al., 2017).

Appendix B: Fast crack limit (Pe ≫ 1) by a crack-tip model

Similar to the previous studies (Noselli et al., 2016; Yu et al., 2018b), a crack-tip model may be constructed for the fast crack limit with $l_{SS} \ll h$, where the elastic crack-tip solution can be applied as the boundary condition. Under plane stress conditions, the displacements in the elastic K-field

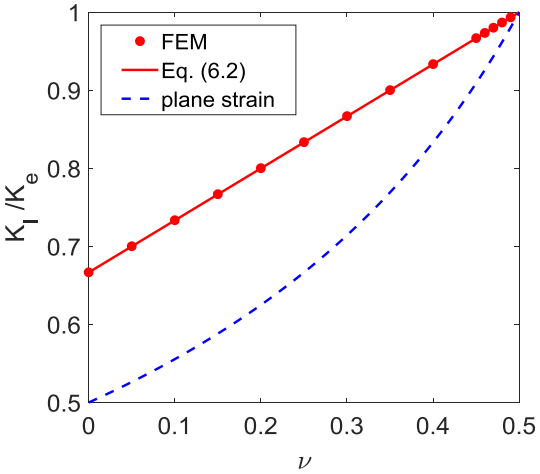

Fig. 17. Effect of Poisson's ratio on the stress intensity factor by the crack-tip model, comparing plane stress and plane strain.

are (Rice, 1968):

$$u_1 = \frac{K_e}{2G}\sqrt{\frac{r}{2\pi}}\cos\left(\frac{\theta}{2}\right)\left[\alpha - 1 + 2\sin^2\left(\frac{\theta}{2}\right)\right], \tag{B.1}$$

$$u_2 = \frac{K_e}{2G}\sqrt{\frac{r}{2\pi}}\sin\left(\frac{\theta}{2}\right)\left[\alpha + 1 - 2\cos^2\left(\frac{\theta}{2}\right)\right], \tag{B.2}$$

where $\alpha = (3-\nu)/(1+\nu)$. For gels, the elastic K-field exists only in a transition region beyond the poroelastic crack-tip field (see Fig. 4), where the solvent concentration remains a constant ($c = c_0$) and the gel is effectively incompressible ($\nu = 0.5$). Thus, we have $\alpha = 5/3$. In addition, the chemical potential in the elastic K-field is obtained in Eq. (6.1), which satisfies the boundary conditions on the crack faces for the immersed case. For the not-immersed case, the elastic K-field is strictly not applicable. Nevertheless, the numerical results (Fig. 3a and Fig. 6) suggest that the stress intensity factor and the energy release rate approach the same fast crack limits for both the immersed and not-immersed cases. In the crack-tip model, we apply the boundary conditions in terms of the displacement and chemical potential for the immersed case only.

The finite element mesh for the crack-tip model is the same as that in the previous study (Yu et al., 2018b). The displacement boundary conditions are applied at the circular outer boundary ($r = nl_{SS}$ and $n > 10$) using Eqs. (B.1) and (B.2) with a stress intensity factor K_e. Similarly, the chemical potential at the outer boundary is set by Eq. (6.1). Therefore, K_e is the single loading parameter in the crack-tip model, and the resulting crack-tip stress intensity factor is linearly proportional to K_e. Hence, in the fast crack limit (Pe $\gg$ 1), the crack-tip model predicts that $K_I/K_e = f(\nu)$, where the effect of Poisson's ratio is found to follow Eq. (6.2) as shown in Fig. 17. Correspondingly, by Eq. (4.9), the crack-tip energy release rate at the fast crack limit is:

$$J^* = \frac{2}{3}(1+\nu)J_e. \tag{B.3}$$

Appendix C: Slow crack limit (Pe $\ll$ 1) by a 1D model

For the slow crack limit, $l_{SS} \gg h$ and the solvent diffusion is primarily one-dimensional (1D) in the x_1 direction. Interestingly, it is found that the approximate 1D model for the slow crack limit under plane stress conditions (immersed or not) is the same as the 1D model under plane strain conditions in the previous study (Yu et al., 2018b). In particular, the chemical potential for $x_1 > 0$ is obtained from the 1D model as

$$\mu(x_1) = \mu_\infty\left[1 - \exp\left(-\frac{x_1}{2(1-\nu)l_{ss}}\right)\right], \tag{C.1}$$

where $\mu_\infty = -2\Omega G\varepsilon_\infty$. The opening stress ahead of the crack tip is:

$$\sigma_{22}(x_1) = 4G\varepsilon_\infty\left[1 - \frac{1-2\nu}{2(1-\nu)}\exp\left(-\frac{x_1}{2(1-\nu)l_{ss}}\right)\right]. \tag{C.2}$$

The predictions by Eqs. (C.1)-(C.2) compare closely with the numerical results in the region $x_1 > h$ for the cases with $h < l_{SS}$ (Pe < 1), as shown in Fig. 5. Note that, because $D_s^* = \frac{D^*}{2(1-\nu)}$ and $l_{ss} = D_s^*/\dot{a}$, the steady-state diffusion length under plane strain is: $2(1-\nu)l_{ss}$.

With the 1D approximation, the crack-tip energy release rate can be calculated by the modified J-integral for the slow crack limit (Pe $\ll$ 1) as:

$$J^* = \frac{2G\varepsilon_\infty^2 h}{1-\nu} = \frac{J_e}{2(1-\nu)}, \tag{C.3}$$

where $J_e = 4G\varepsilon_\infty^2 h$. Correspondingly, the slow crack limit of the stress intensity factor under plane stress is:

$$K_I = \sqrt{\tilde{E}J^*} = 2G\varepsilon_\infty\sqrt{\frac{(1+\nu)h}{1-\nu}}. \tag{C.4}$$

References

Atkinson, C., Craster, R.V., 1991. Plane strain fracture in poroelastic media. Proc. R. Soc. Lond. A 434, 605–633.

Balay, S., Abhyankar, S., Adams, M.F., Brown, J., Brune, P., Buschelman, K., Dalcin, L., Eijkhout, V., Gropp, W.D., Kaushik, D., Knepley, M.G., McInnes, L.C., Rupp, K., Smith, B.F., Zampini, S., Zhang, H., 2017. PETSc users manual. Argonne Natl. Lab ANL-95/11 - Revision 3.8.

Bao, G., Suo, Z., 1992. Remarks on crack-bridging concepts. Appl. Mech. Rev. 45, 355–366.

Baumberger, T., Caroli, C., Martina, D., 2006. Solvent control of crack dynamics in a reversible hydrogel. Nat. Mater. 5, 552–555.

Biot, M.A., 1941. General theory of three-dimensional consolidation. J. Appl. Phys. 12, 155–164.

Bouklas, N., Huang, R., 2012. Swelling kinetics of polymer gels: comparison of linear and nonlinear theories. Soft Matter 8, 8194–8203.

Bouklas, N., Landis, C.M., Huang, R., 2015. Effect of solvent diffusion on crack-tip fields and driving force for fracture of hydrogels. J. Appl. Mech. 82, 081007.

Brooks, A.N., Hughes, T.J.R., 1982. Streamline upwind Petrov-Galerkin formulations for convection dominated flows with particular emphasis on the incompressible Navier-Stokes equations. Comput. Meth. Appl. Mech. Eng. 32, 199–259.

Creton, C., 2017. 50th Anniversary perspective: networks and gels: soft but dynamic and tough. Macromolecules 50, 8297–8316.

Forte, A.E., D'Amico, F., Charalambides, M.N., Dini, D., Williams, J.G., 2015. Modelling and experimental characterisation of the rate dependent fracture properties of Gelatine gels. Food Hydrocoll. 46, 180–190.

Franca, L.P., Frey, S.L., Hughes, T.J.R., 1992. Stabilized finite-element methods 1. Application to the advective-diffusive model. Comput. Meth. Appl. Mech. Eng. 95, 253–276.

Franca, L.P., Hauke, G., Masud, A., 2006. Revisiting stabilized finite element methods for the advective-diffusive equation. Comput. Meth. Appl. Mech. Eng. 195, 1560–1572.

Gong, J.P., Katsuyama, Y., Kurokawa, Y., Osada, Y., 2003. Double-network hydrogels with extremely high mechanical strength. Adv. Mater. 15, 1155–1158.

Guo, J., Liu, M., Zehnder, A.T., Zhao, J., Narita, T., Creton, C., Hui, C.-Y., 2018. Fracture mechanics of a self-healing hydrogel with covalent and physical crosslinks: a numerical study. J. Mech. Phys. Solids 120, 79–95.

Hong, W., Zhao, X., Zhou, J., Suo, Z., 2008. A theory of coupled diffusion and large deformation in polymeric gels. J. Mech. Phys. Solids 56, 1779–1793.

Hu, Y., Chen, X., Whitesides, G.M., Vlassak, J.J., Suo, Z., 2011. Indentation of polydimethylsiloxane submerged in organic solvents. J. Mater. Res. 26, 785.

Hui, C.-Y., Lin, Y.Y., Chuang, F.-C., Shull, K.R., Lin, W.-C., 2006. A contact mechanics method for characterizing the elastic properties and permeability of gels. J. Polym. Sci., Part B 44, 359–370.

Hui, C.Y., Long, R., Ning, J., 2013. Stress relaxation near the tip of a stationary mode I crack in a poroelastic solid. J. Appl. Mech. 80, 021014.

Hutchinson, J.W., Evans, A.G., 2000. Mechanics of materials: top-down approaches to fracture. Acta Mater 48, 125–135.

Kang, M.K., Huang, R., 2010. A variational approach and finite element implementation for swelling of polymeric hydrogels under geometric constraints. J. Appl. Mech. 77, 061004.

Lefranc, M., Bouchaud, E., 2014. Mode I fracture of a biopolymer gel: rate-dependent dissipation and large deformations disentangled. Extreme Mech. Lett. 1, 97–103.

Li., S., Wang, J., Thouless, M.D., 2004. The effects of shear on delamination in layered materials. J. Mech. Phys. Solids 52, 193–214.

Liu, M., Guo, J., Hui, C.-Y., Zehnder, A.T., 2019. Crack tip stress based kinetic fracture model of a PVA dual-crosslink hydrogel. Extreme Mech. Lett 29, 100457.

Long, R., Hui, C.-Y., 2016. Fracture toughness of hydrogels: measurement and interpretation. Soft Matter 12, 8069–8086.

Long, R., Lefranc, M., Bouchaud, E., Hui, C.-Y., 2016. Large deformation effect in Mode I crack opening displacement of an Agar gel: a comparison of experiment and theory. Extreme Mech. Lett. 9, 66–73.

Mao, Y., Anand, L., 2018. A theory for fracture of polymeric gels. J. Mech. Phys. Solids 115, 30–53.

Noselli, G., Lucantonio, A., McMeeking, R.M., DeSimone, A., 2016. Poroelastic toughening in polymer gels: a theoretical and numerical study. J. Mech. Phys. Solids 94, 33–46.

Rice, J.R., 1968. Mathematical analysis in the mechanics of fracture. In: Liebowitz, H. (Ed.), Fracture: An Advanced Treatise (vol. 2, Mathematical Fundamentals). Academic Press, N.Y., pp. 191–311.

Rivlin, R.S., Thomas, A.G., 1953. Rupture of rubber. I. Characteristic energy for tearing. J. Poly. Sci. 3, 291–318.

Seitz, M.E., Martina, D., Baumberger, T., Krishnan, V.R., Hui, C.Y., Shull, K.R., 2009. Fracture and large strain behavior of self-assembled triblock copolymer gels. Soft Matter 5, 447–456.

Sun, J.-Y., Zhao, X., Illeperuma, W.R.K., Chaudhuri, O., Oh, K.H., Mooney, D.J., Vlassak, J.J., Suo, Z., 2012. Highly stretchable and tough hydrogels. Nature 489, 133–136.

Wang, X., Hong, W., 2012. Delayed fracture in gels. Soft Matter 8, 8171–8178.

Yang, C.-H., Lin, Y.-Y., 2018. Time-dependent fracture of mode-I cracks in poroviscoelastic media. Eur. J. Mech. A 69, 78–87.

Yu, Y., Bouklas, N., Landis, C.M., Huang, R., 2018a. A linear poroelastic analysis of time-dependent crack-tip fields in polymer gels. J. Appl. Mech. 85, 111011.

Yu, Y., Landis, C.M., Huang, R., 2018b. Steady-state crack growth in polymer gels: a linear poroelastic analysis. J. Mech. Phys. Solids 118, 15–39.

Zhao, X., 2014. Multi-scale multi-mechanism design of tough hydrogels: building dissipation into stretchy networks. Soft Matter 10, 672–687.